Supplementary Information (SI) for

Seismic detection of a deep mantle discontinuity within Mars by InSight

Authors: Quancheng Huang[1,2]*, Nicholas C. Schmerr[1], Scott D. King[3], Doyeon Kim[1,4], Attilio Rivoldini[5], Ana-Catalina Plesa[6], Henri Samuel[7], Ross R. Maguire[1], Foivos Karakostas[1,8], Vedran Lekić[1], Constantinos Charalambous[9], Max Collinet[6], Robert Myhill[10], Daniele Antonangeli[11], Mélanie Drilleau[12], Misha Bystricky[13], Caroline Bollinger[13], Chloé Michaut[14], Tamara Gudkova[15], Jessica C.E. Irving[10], Anna Horleston[10], Benjamin Fernando[16], Kuangdai Leng[16], Tarje Nissen-Meyer[16], Frederic Bejina[13], Ebru Bozdağ[2], Caroline Beghein[17], Lauren Waszek[18], Nicki C. Siersch[11], John-Robert Scholz[19], Paul M. Davis[17], Philippe Lognonné[7], Baptiste Pinot[12], Rudolf Widmer-Schnidrig[20], Mark P. Panning[21], Suzanne E. Smrekar[21], Tilman Spohn[6], William T. Pike[9], Domenico Giardini[4], W. Bruce Banerdt[21]

*Corresponding author: Quancheng Huang. Email: qchuang@umd.edu

Affiliations:

1. Department of Geology, University of Maryland, College Park, Maryland, USA

2. Department of Geophysics, Colorado School of Mines, Golden, Colorado, USA

3. Department of Geosciences, Virginia Tech, Blacksburg, Virginia, USA

4. Institute of Geophysics, ETH Zurich, Zurich, Switzerland

5. Royal Observatory of Belgium, Brussels, Belgium

6. Institute of Planetary Research, German Aerospace Center (DLR), Berlin, Germany

7. Université de Paris, Institut de Physique du Globe de Paris, CNRS, Paris, France

8. Istituto Nazionale di Geofisica e Vulcanologia, Sezione di Bologna, Bologna, Italy

9. Department of Electrical and Electronic Engineering, Imperial College London, London, United Kingdom

10. School of Earth Sciences, University of Bristol, Bristol, United Kingdom

11. Sorbonne Université, Muséum National d'Histoire Naturelle, UMR CNRS 7590, Institut de Minéralogie, de Physique des Matériaux et de Cosmochimie, IMPMC, Paris, France

12. Institut Supérieur de l'Aéronautique et de l'Espace SUPAERO, Toulouse, France

13. Institut de Recherche en Astrophysique et Planétologie, Université Toulouse III Paul Sabatier, CNRS, Toulouse, France

14. Université de Lyon, École Normale Supérieure de Lyon, UCBL, CNRS, Laboratoire de Géologie de Lyon -Terre, Planètes, Environnement, Lyon, France

15. Schmidt Institute of Physics of the Earth RAS, Moscow, Russia

16. Department of Earth Sciences, University of Oxford, Oxford, United Kingdom

17. Department of Earth, Planetary, and Space Sciences, University of California, Los Angeles, California, USA

18. Physical Sciences Group, James Cook University, Douglas, Queensland, Australia

19. Max Planck Institute for Solar System Research, Göttingen, Germany

20. Black Forest Observatory, Stuttgart University, Germany

21. Jet Propulsion Laboratory, California Institute of Technology, Pasadena, California, USA

This PDF file includes:

Supplementary text

Figures S1-1 to S5-4

Tables S1-1 to S5-3

SI References

Table of Contents

SI1. Supplementary Figures and Tables for Methods of Seismic Data Analysis

Table S1-1. Summary of $t_S - t_P$, back-azimuths and SNR of the LF and BB events. SNR_P and SNR_S represent the SNR of P and S waves respectively.

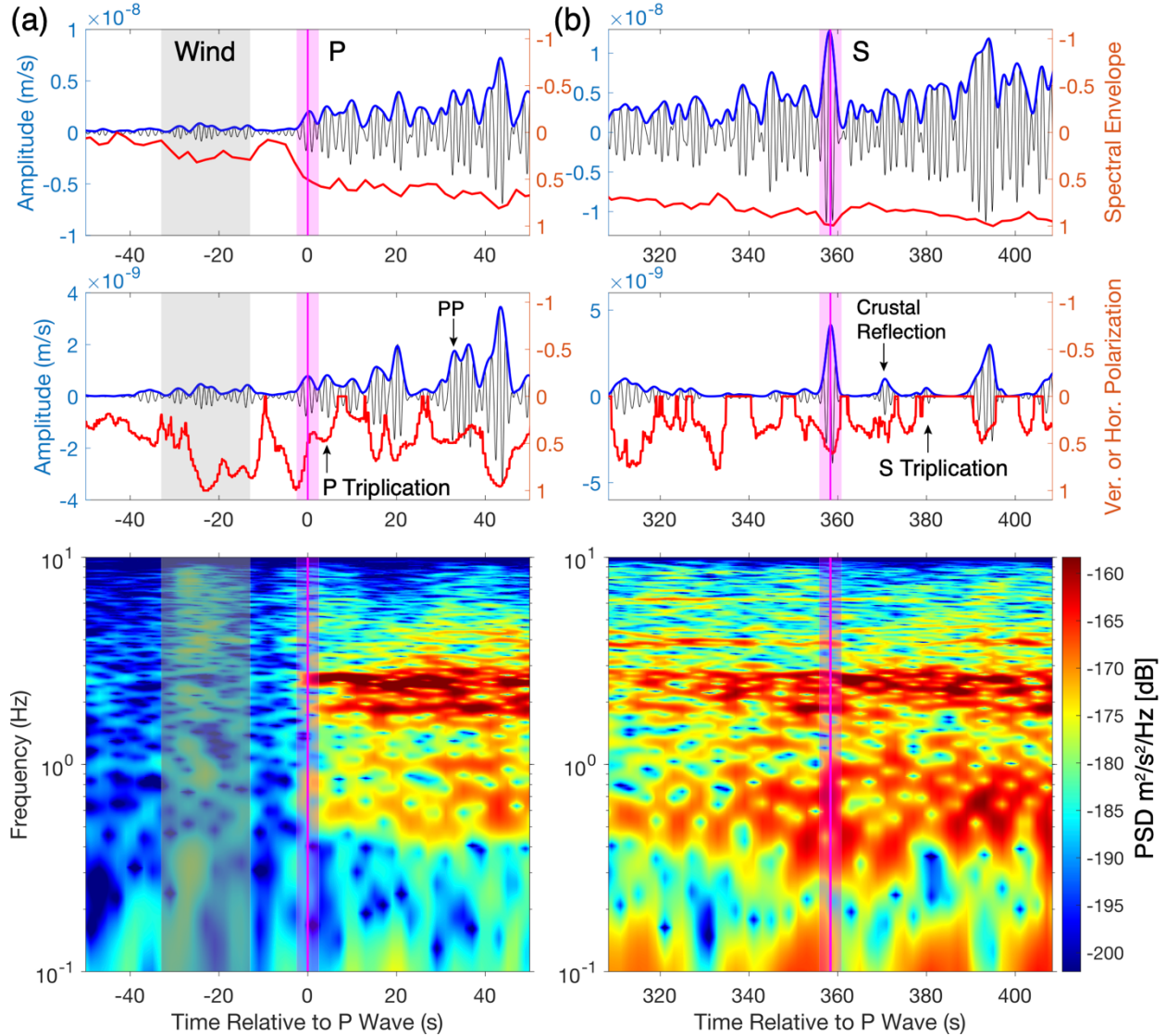| Event	Type	Quality	$t_S - t_P$ (s)	Back-azimuth (degree)	SNR_P	SNR_S
S1094b	BB	A	358.4±5.0	35.9±6.5	7.3	51.4
S1102a	BB	B	410.2±10.0	92.0±42.2	7.4	10.9
S0185a	BB	B	360.4±7.5	161.0±8.2	4.0	12.3
S0234c	LF	C	394.9±10.0	258.5±72.1	2.3	3.4
S0345a	LF	C	373.6±10.0	179.0±12.1	2.2	3.6

Fig. S1-1. Bandpass filtered waveforms (top), polarization analyses (middle) and spectrograms (bottom) of S1094b event. The first and second columns show the (a) P-wave on the vertical component and (b) S-wave on the radial component, respectively. The first row shows the raw data band-pass filtered between 0.5-0.9 Hz in black and the corresponding envelopes in blue. The spectral envelopes, which are computed from the average amplitudes on spectrograms between 0.5-0.9 Hz, are shown in red with a reversed y-axis. Pink lines highlight the P- and S-arrival picks and the pink shaded regions indicate their uncertainties (± 2.5 s). The gray shaded regions indicate the time windows contaminated by wind or instrumental glitches. The second row shows the polarization filtered waveforms in black and the corresponding envelopes in blue. The red curves show the vertical polarization attributes for P-wave and horizontal polarization attributes for S-wave from the Frequency Dependent Polarization Analysis (FDPA). Note that the y-axis is reversed for FDPA. Body waves are identified using the post-landing models (1–3) and highlighted in black arrows. The third row shows the spectrograms. The SNR of S-wave are 51.4 and 26.1 on the radial and transverse components respectively. Therefore, the S-arrival pick is made on the radial component here.
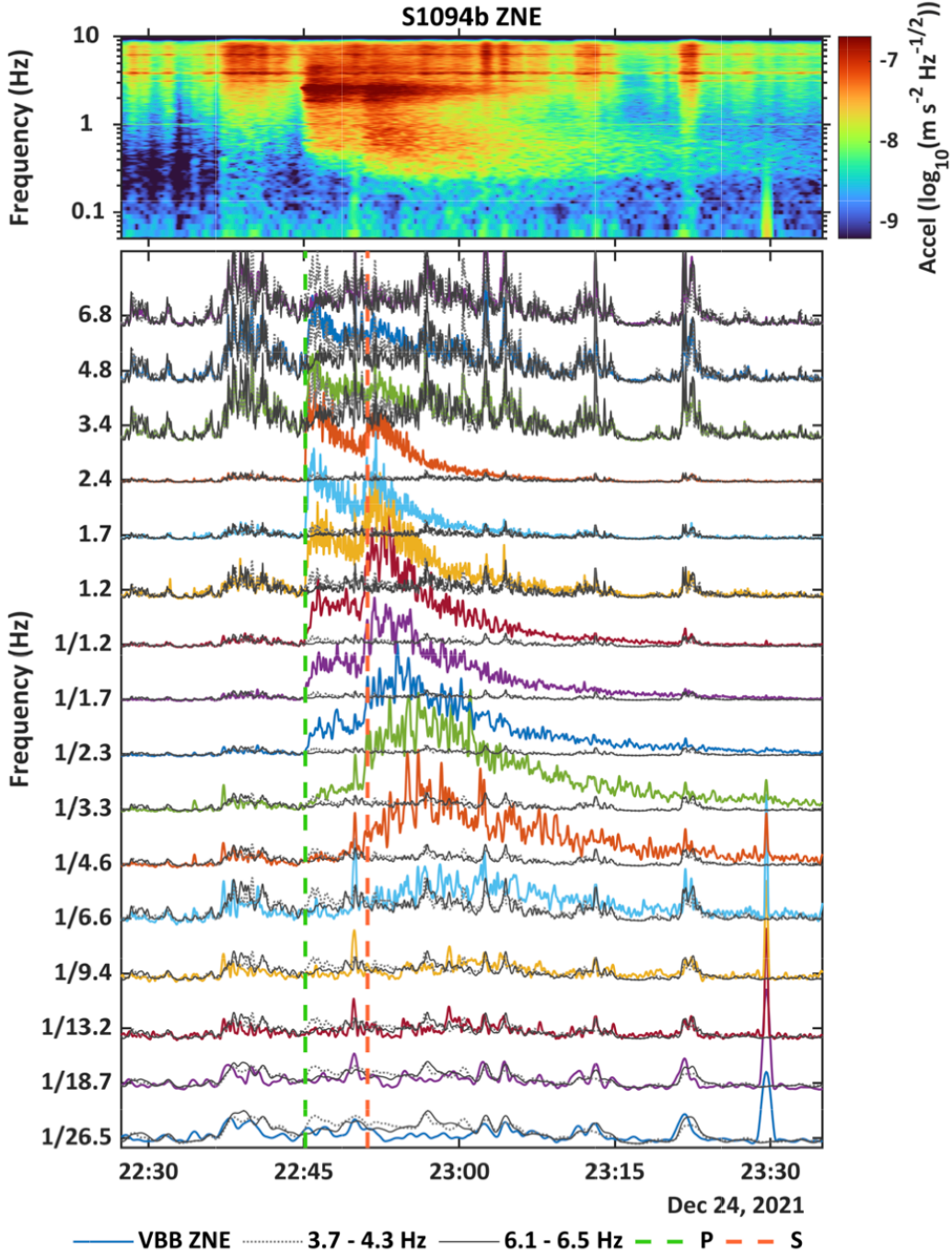
6

Fig. S1-2. Comodulation analysis of S1094b event. Top panel: combined energy spectrogram for VBB ZNE 20 sps data. Lower panel: VBB ZNE power envelopes (color lines) in different frequency bands, and VBB ZNE power between 3.7 – 4.3 Hz (dotted line) and 6.1 – 6.5 Hz (solid line). Pressure and wind data were not available for this event. We therefore use the power around the known weather-sensitive lander modes at 4 Hz and 6.3 Hz as proxies for atmospheric injection. P and S picks as derived in the main text are marked by vertical green and red dashed lines respectively. Note the divergence of the seismic power from the expected noise injected by the local atmosphere.
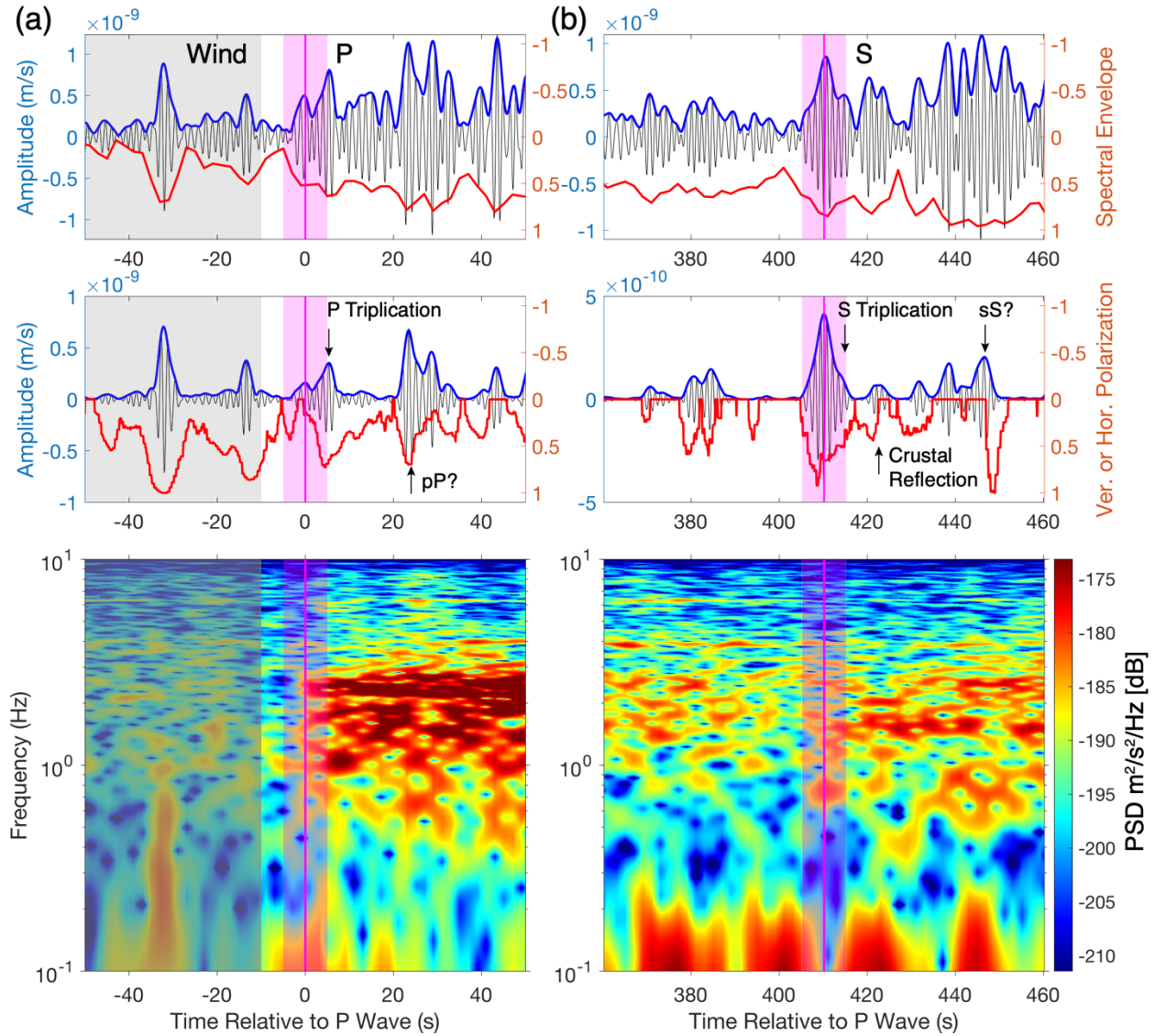
Fig. S1-3. Bandpass filtered waveforms (top), polarization analyses (middle) and spectrograms (bottom) of S1102a event. The first and second columns show the (a) P-wave on the vertical component and (b) S-wave on the radial component, respectively. The first row shows the raw data band-pass filtered between 0.5-0.9 Hz. The second row shows the polarization filtered waveforms and the vertical (left) or horizontal (right) polarization attributes from FDPA. The third row shows the spectrograms. Legends are the same as Fig. S1-1. The SNR of S-wave are 5.6 and 10.9 on the transverse and radial components respectively. Therefore, the S-arrival pick is made on the radial component here. The uncertainties for P- and S-arrival picks are 5 s.
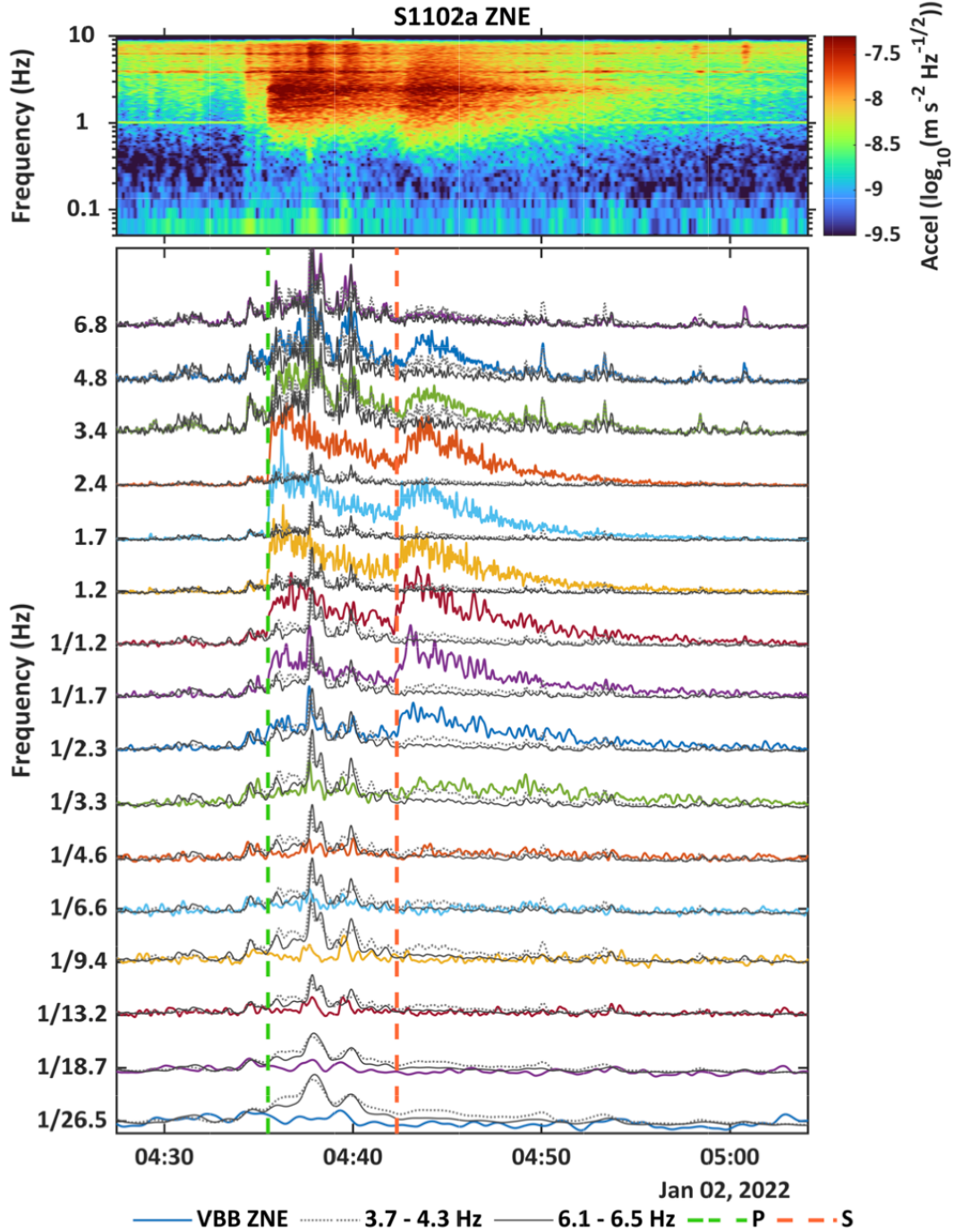
Fig. S1-4. Comodulation analysis of S1102a event. Top panel: combined energy spectrogram for VBB ZNE 20 sps data. Lower panel: VBB ZNE power envelopes (color lines) in different frequency bands, and VBB ZNE power between 3.7 – 4.3 Hz (dotted line) and 6.1 – 6.5 Hz (solid line). Pressure and wind data were not available for this event. We therefore used the power around the known weather-sensitive lander modes at 4 Hz and 6.3 Hz as proxies for atmospheric injection. P and S picks as derived in the main text are marked by vertical green and red dashed lines respectively. Note the clear divergence of the seismic power from the proxy for atmospheric power across multiple frequency bands for both P and S phases.
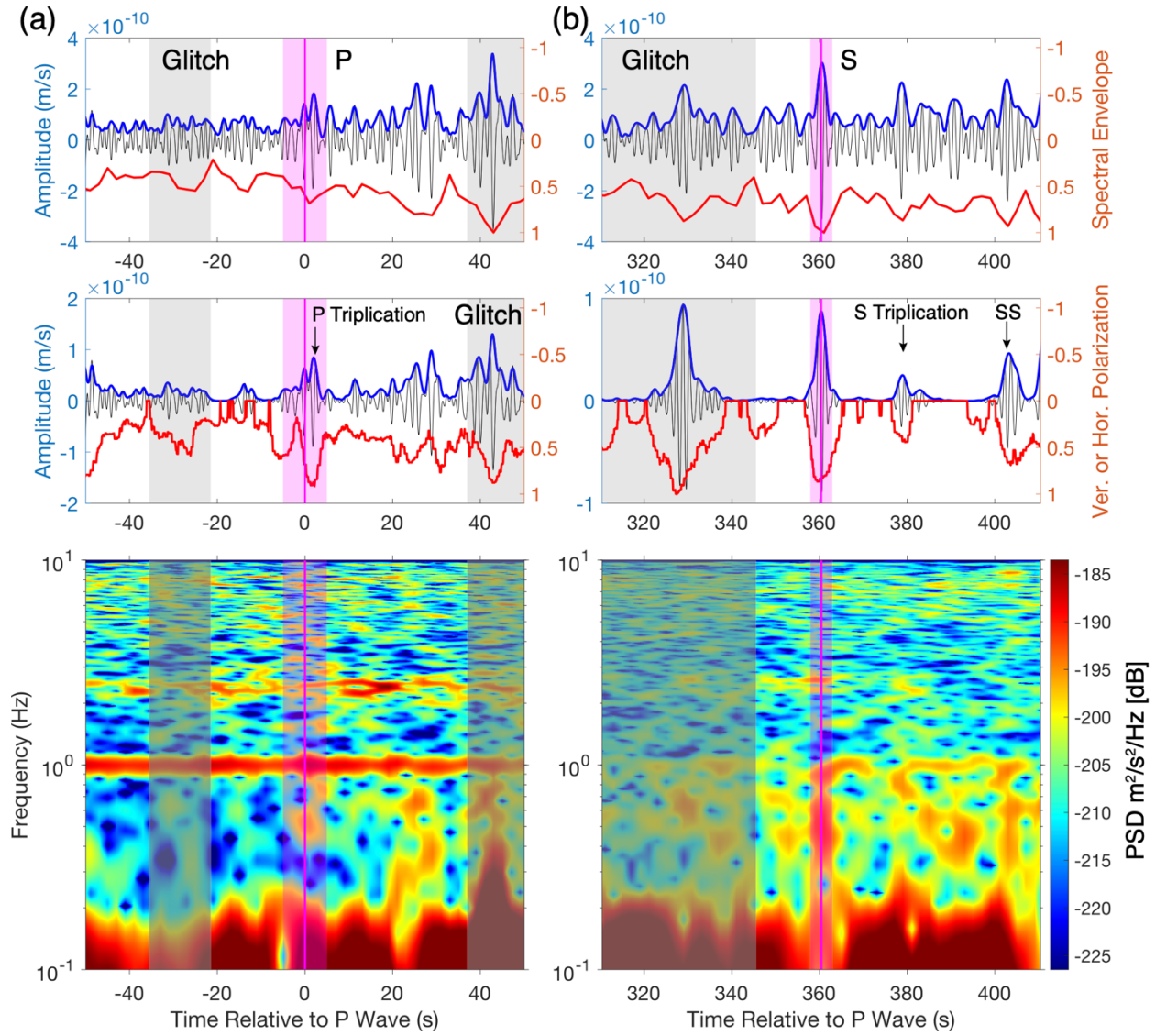
Fig. S1-5. Bandpass filtered waveforms (top), polarization analyses (middle) and spectrograms (bottom) of S0185a event. The first and second columns show the (a) P-wave on the vertical component and (b) S-wave on the transverse component, respectively. The first row shows the raw data band-pass filtered between 0.3-0.9 Hz for P-wave and 0.5-0.9 Hz for S-wave. The second row shows the polarization filtered waveforms and the vertical (left) or horizontal (right) polarization attributes from FDPA. The third row shows the spectrograms. Legends are the same as Fig. S1-1. The SNR of S-wave are 12.3 and 4.0 on the transverse and radial components respectively. Therefore, the S-arrival pick is made on the transverse component here. The uncertainties for P- and S-arrival picks are 5 s and 2.5 s, respectively.

Fig. S1-6. Comodulation analysis of S0185a event. Top panel: combined energy spectrogram for VBB ZNE 20 sps data. Lower panel: Filter bank of the combined ZNE seismic power envelopes (color lines) and pressure envelopes at a range of frequencies, with both moment-matched to the wind speed time series (gray). P and S picks as derived in the main text are marked by vertical green and red dashed lines respectively. The energy of this event is in clear excess of the noise predicted by both wind and pressure data.
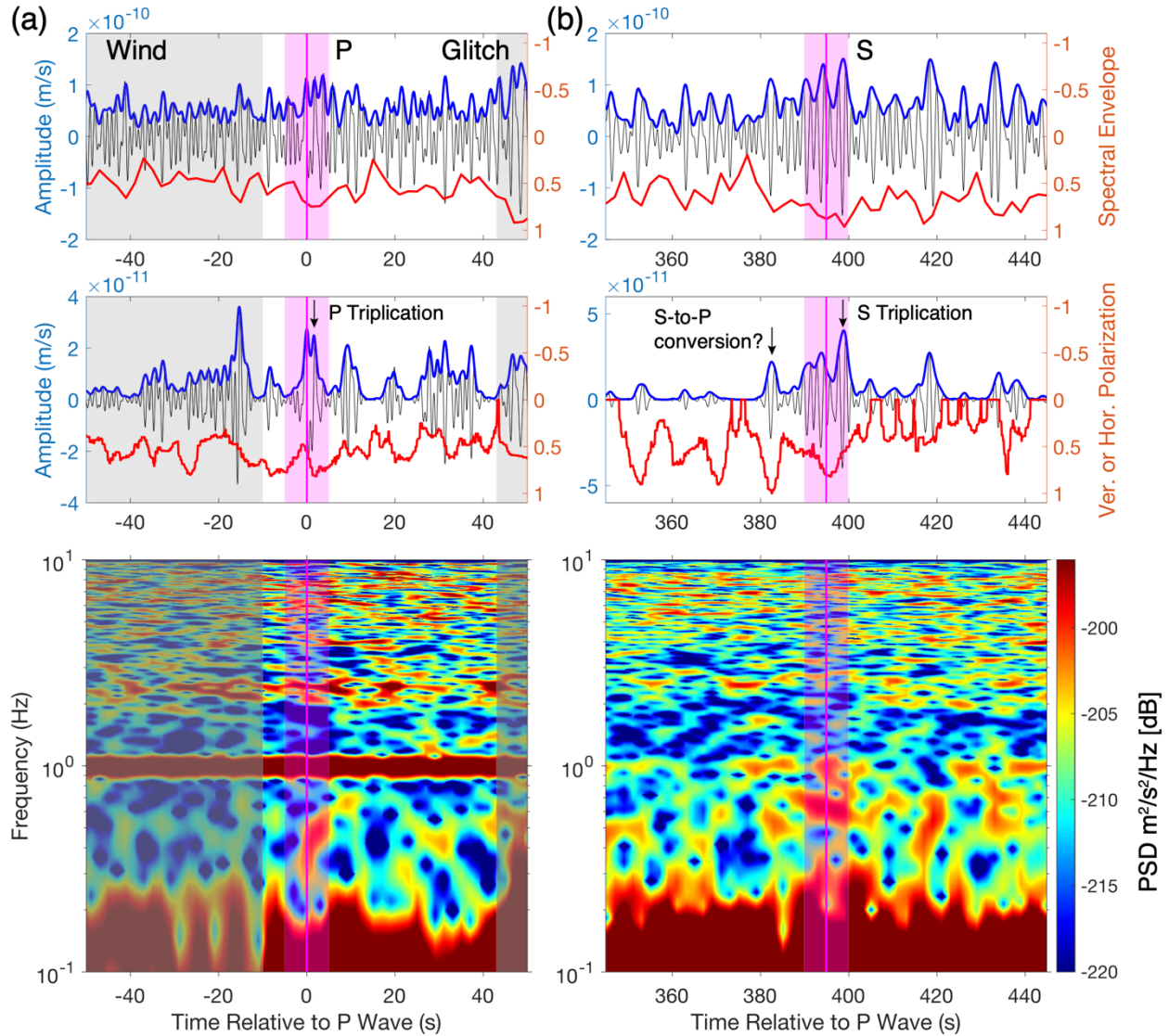
Fig. S1-7. Bandpass filtered waveforms (top), polarization analyses (middle) and spectrograms (bottom) of S0234c event. The first and second columns show the (a) P-wave on the vertical component and (b) S-wave on the radial component, respectively. The first row shows the raw data band-pass filtered between 0.3-0.9 Hz. The second row shows the polarization filtered waveforms and the vertical or horizontal polarization attributes from FDPA. The third row shows the spectrograms. Legends are the same as Fig. S1-1. The SNR of S-wave are 2.2 and 3.4 on the transverse and radial components respectively. Therefore, the S-arrival pick is made on the radial component here, but the transverse component is used for the waveform modeling due to its cleaner waveforms. The uncertainties for P- and S-arrival picks are 5 s.
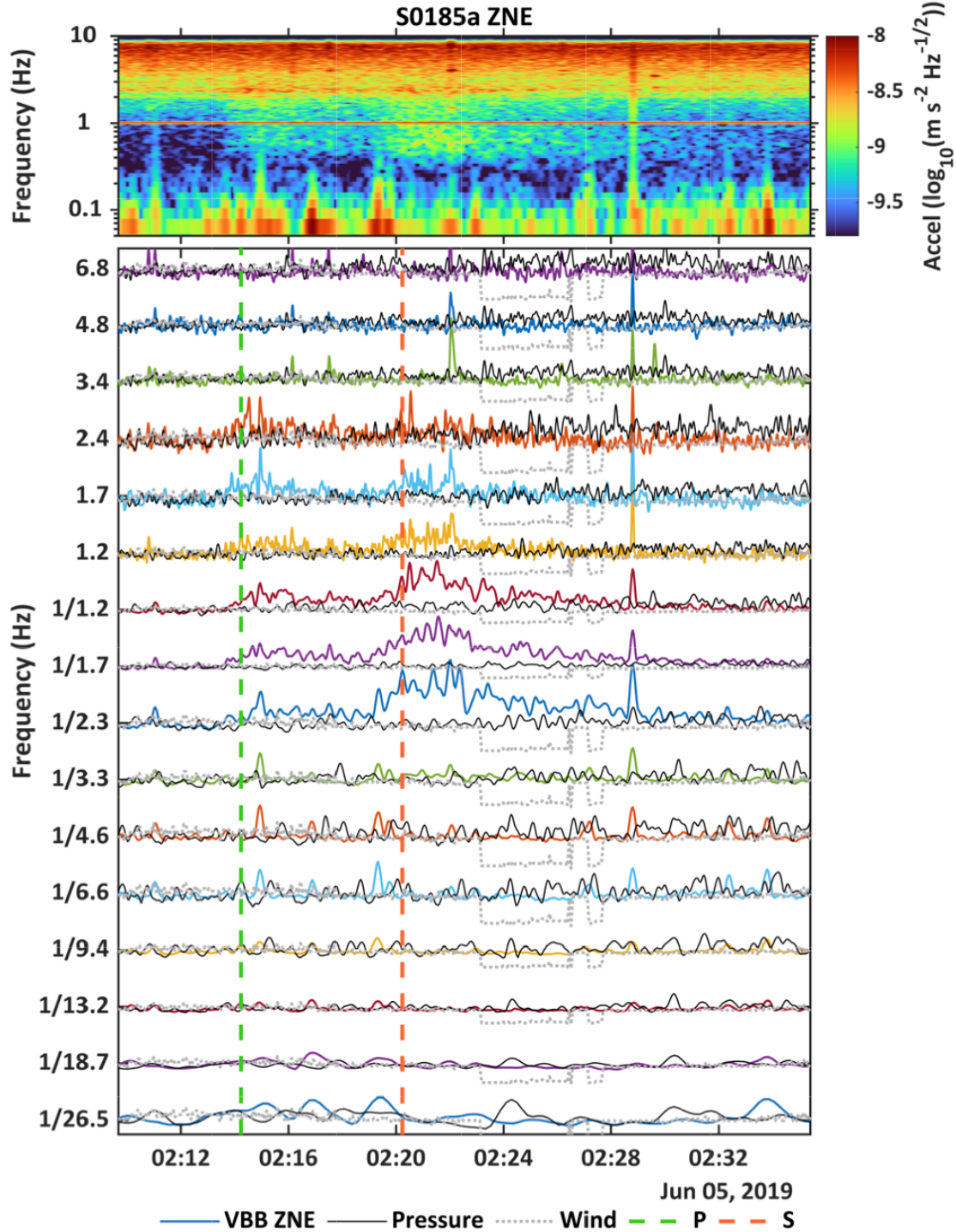
Fig. S1-8. Comodulation analysis of S0234c event. Top panel: combined energy spectrogram for VBB ZNE 20 sps data. Lower panel: Filter bank of the combined ZNE seismic power envelopes (color lines) and pressure envelopes at a range of frequencies, with both moment-matched to the wind speed time series (gray). P and S picks as derived in the main text are marked by vertical green and red dashed lines respectively. The energy in the bandwidth of interest for this event is in excess of the expected noise injected over various frequency bands by the local atmospheric pressure and wind.

13
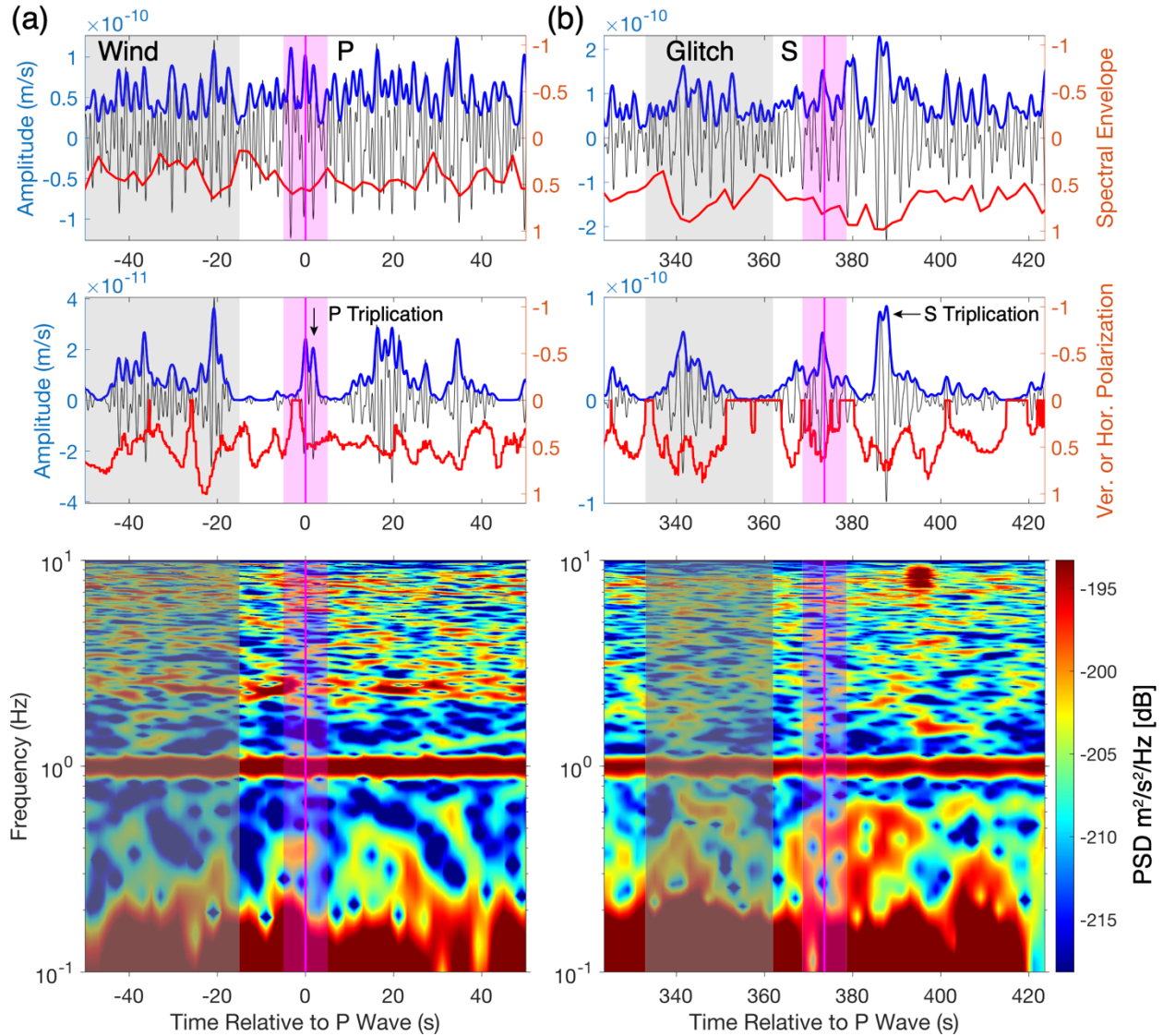
Fig. S1-9. Bandpass filtered waveforms (top), polarization analyses (middle) and spectrograms (bottom) of S0345a event. The first and second columns show the (a) P-wave on the vertical component and (b) S-wave on the radial component, respectively. The first row shows the raw data band-pass filtered between 0.3-0.9 Hz. The second row shows the polarization filtered waveforms and the vertical or horizontal polarization attributes from FDPA. The third row shows the spectrograms. Legends are the same as Fig. S1-1. The SNR of S-wave are 2.5 and 3.6 on the transverse and radial components respectively. Therefore, the S-arrival pick is made on the radial component here. The uncertainties for P- and S-arrival picks are 5 s.
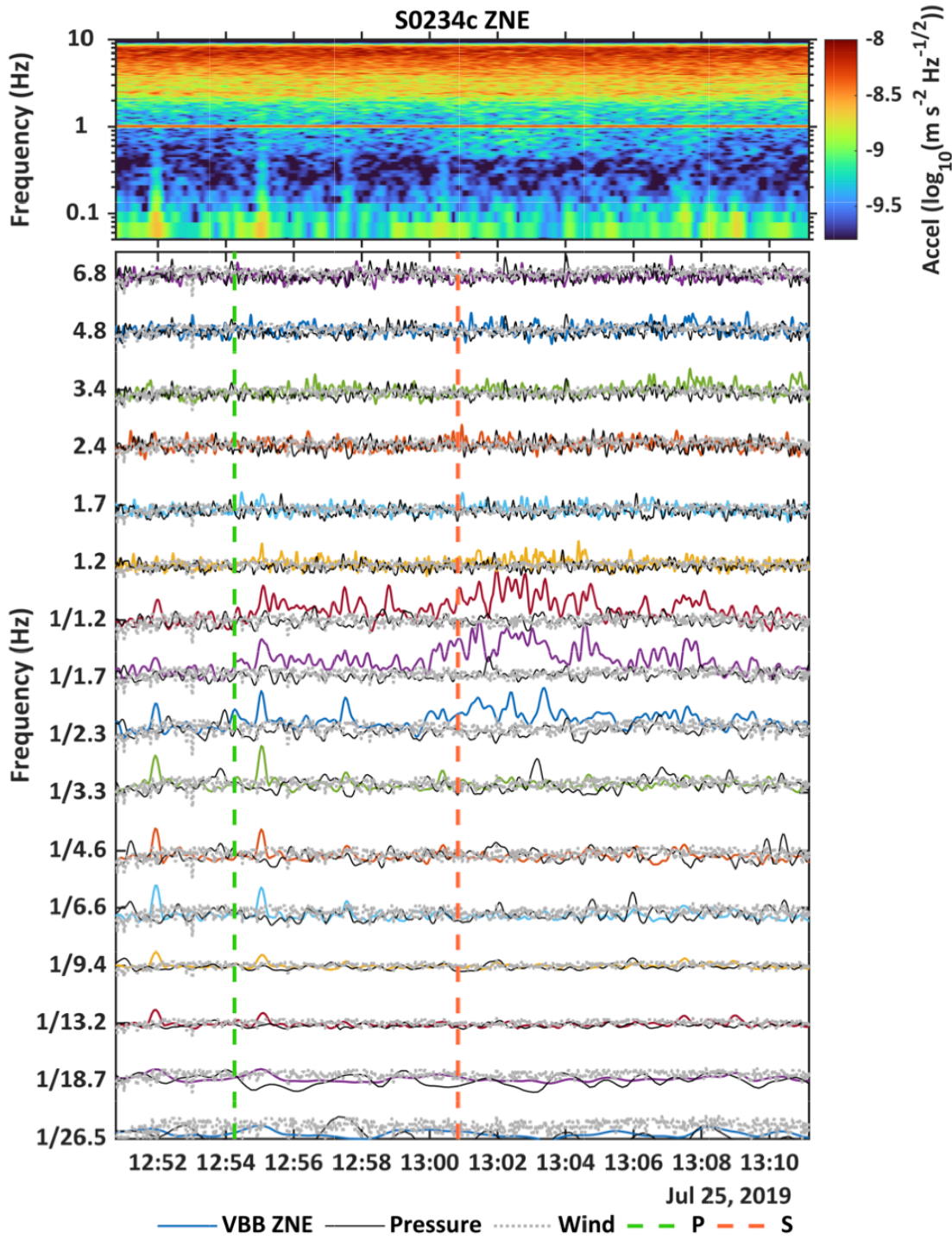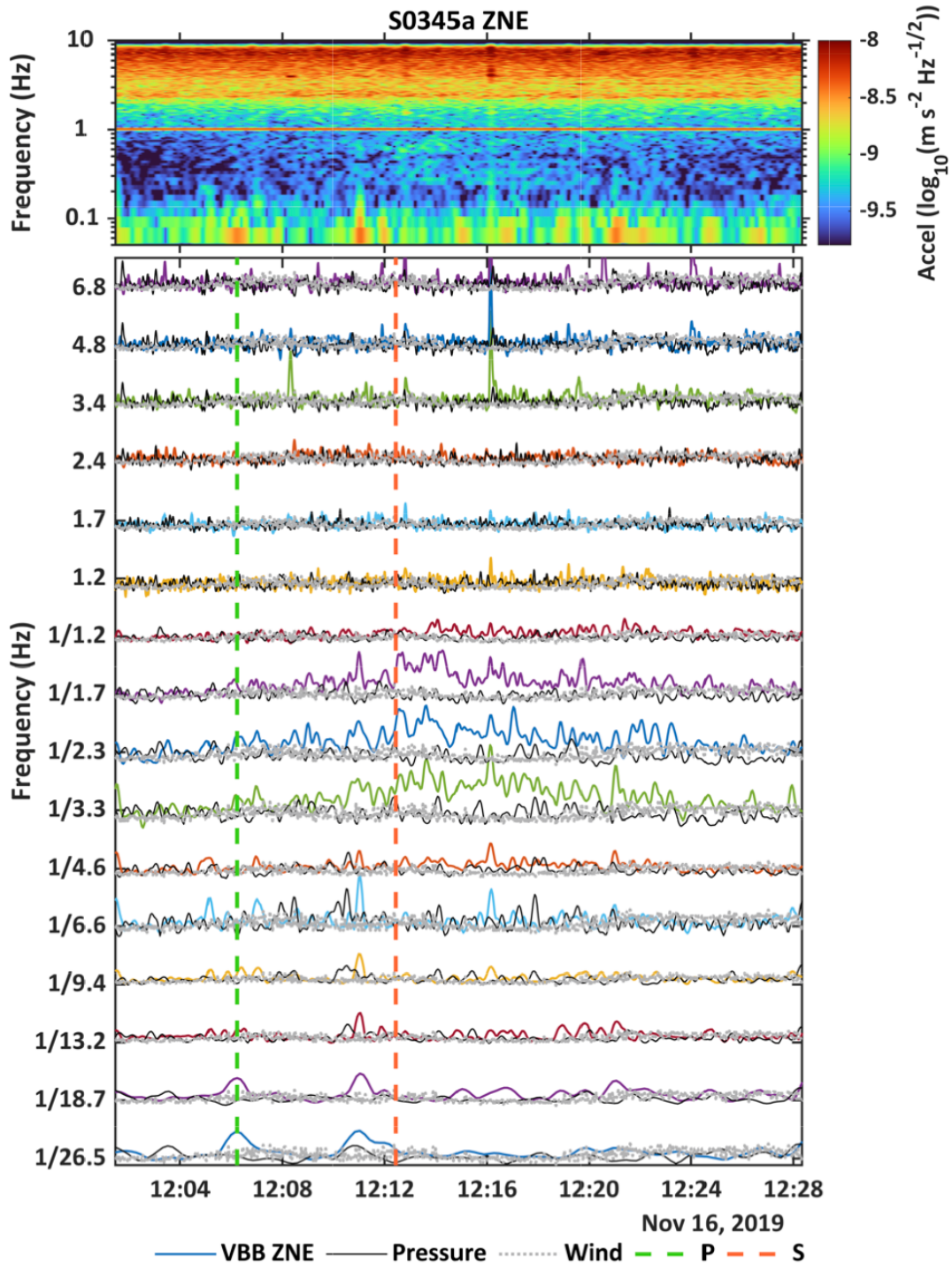
Fig. S1-10. Comodulation analysis of S0345a event. Top panel: combined energy spectrogram for VBB ZNE 20 sps data. Lower panel: Filter bank of the combined ZNE seismic power envelopes (color lines) and pressure envelopes at a range of frequencies, with both moment-matched to the wind speed time series (gray). P and S picks as derived in the main text are marked by vertical green and red dashed lines respectively. The energy in the bandwidth of interest for this event is in excess of the expected noise injected over various frequency bands by the local atmospheric pressure and wind.

15

Fig. S1-11. (a) Comodulation analysis of S0167a event using the weather data. Top panel: combined energy spectrogram for VBB ZNE 20 sps data. Lower panel: Filter bank of the combined ZNE seismic power envelopes (color lines) and pressure envelopes at a range of frequencies, with both moment-matched to the wind speed time series (gray). The arrival of the P phase is uncertain due to lack of excess energy, which only appears later during the putative P phase. In addition, a strong high-frequency pressure burst builds up at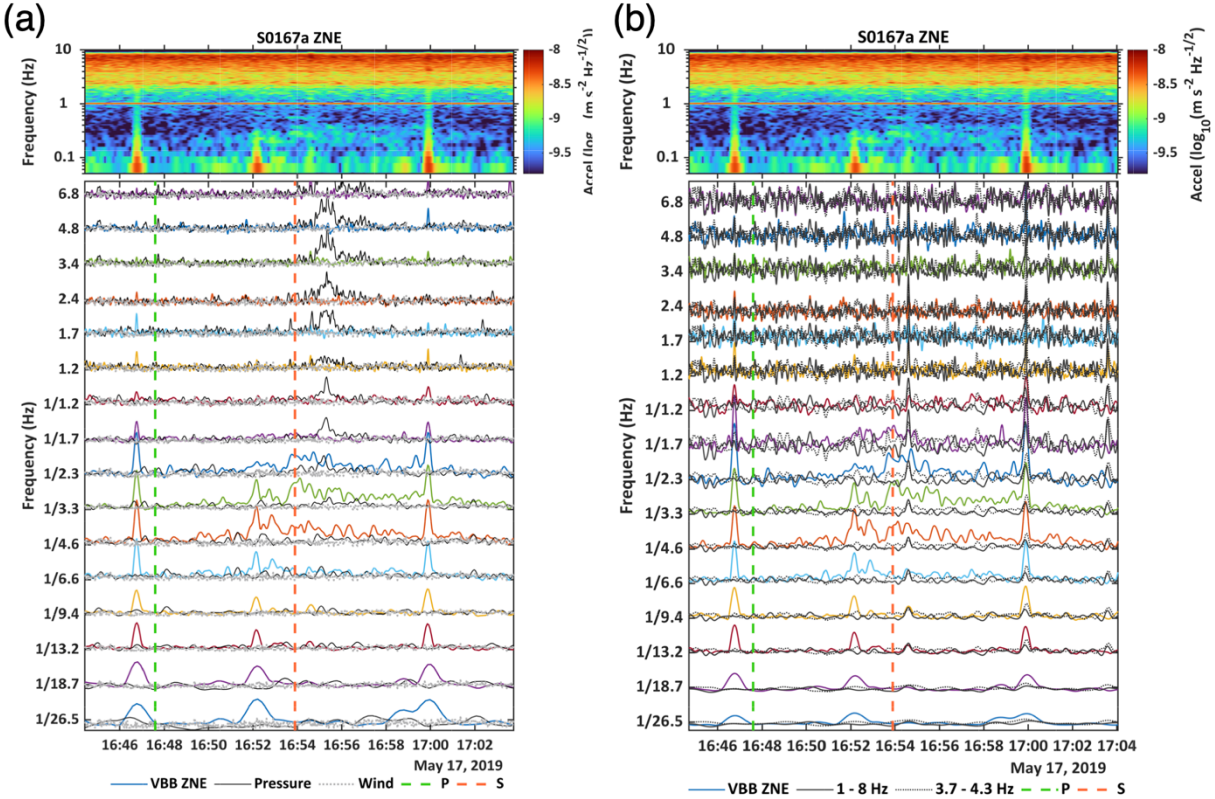 the onset of the S wave. **(b)** Comodulation analysis of S0167a event using the lander modes. Top panel: combined energy spectrogram for VBB ZNE 20 sps data. Lower panel: VBB ZNE power envelopes (color lines) in different frequency bands, and VBB ZNE power between 3.7 – 4.3 Hz (dotted line) and 1 – 8 Hz (solid line). Due to the uncertainties presented above, we also apply comodulation analysis against the ~4 Hz weather-sensitive lander mode. The P phase is heavily contaminated by wind-noise injection and shows excess energy only later during the phase in both weather and lander comodulation analyses. This suggests that the P phase arrival could either be embedded within the environmental noise or have a later arrival time. With this uncertainty, we therefore reject this event as being located within a favorable epicentral distance for mantle triplications.
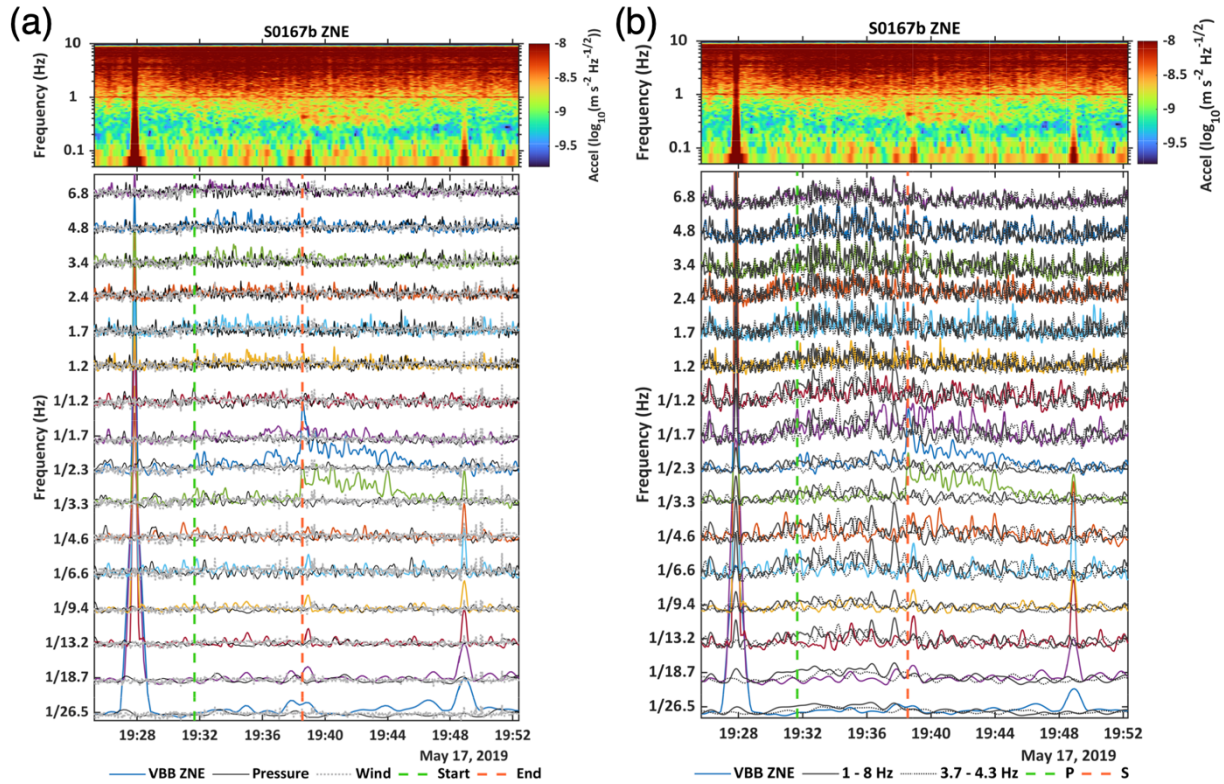
Fig. S1-12. (a) Comodulation analysis of S0167b event using the weather data. Top panel: combined energy spectrogram for VBB ZNE 20 sps data. Lower panel: Filter bank of the combined ZNE seismic power envelopes (color lines) and pressure envelopes at a range of frequencies, with both moment-matched to the wind speed time series (gray). The P phase identified for this event is likely contaminated by the local weather. The excess seismic energy from the atmospheric injection is only clear halfway through the P phase and this could indicate a shorter distance for this event. **(b)** Comodulation analysis of S0167b event using the lander modes. Due to the uncertainties mentioned above, we also apply comodulation analysis against the ~4-Hz weather-sensitive lander mode, and the total broadband noise above > 1 Hz which is known to correlate with the atmospheric injection. Atmospherically-induced lander vibrations during the P phase appear to be contaminating the entire phase; comodulation indicates a good match between the putative P phase and the clear broadband noise injection that coincides during this phase. While the S phase does show clear excess energy from the predicted atmospheric injection, we reject this event being within the favorable epicentral distance for mantle triplications due to heavy contamination by wind noise which likely embeds the P phase within the environmental noise.
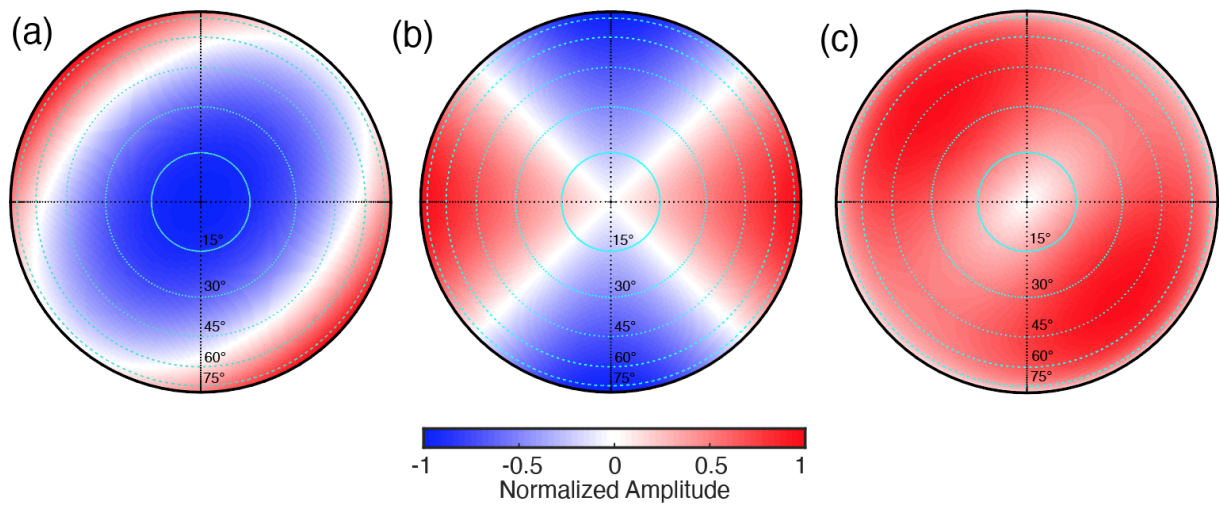
Fig. S1-13. Radiation patterns for the (a) P-wave, (b) SH-wave and (c) SV-wave used as the seismic source for AxiSEM synthetics. Cyan circles denote the take-off angles. The receivers are placed on the equator to the east of the source. This moment tensor was chosen to allow for energy from all three types of waves in the receiver direction.
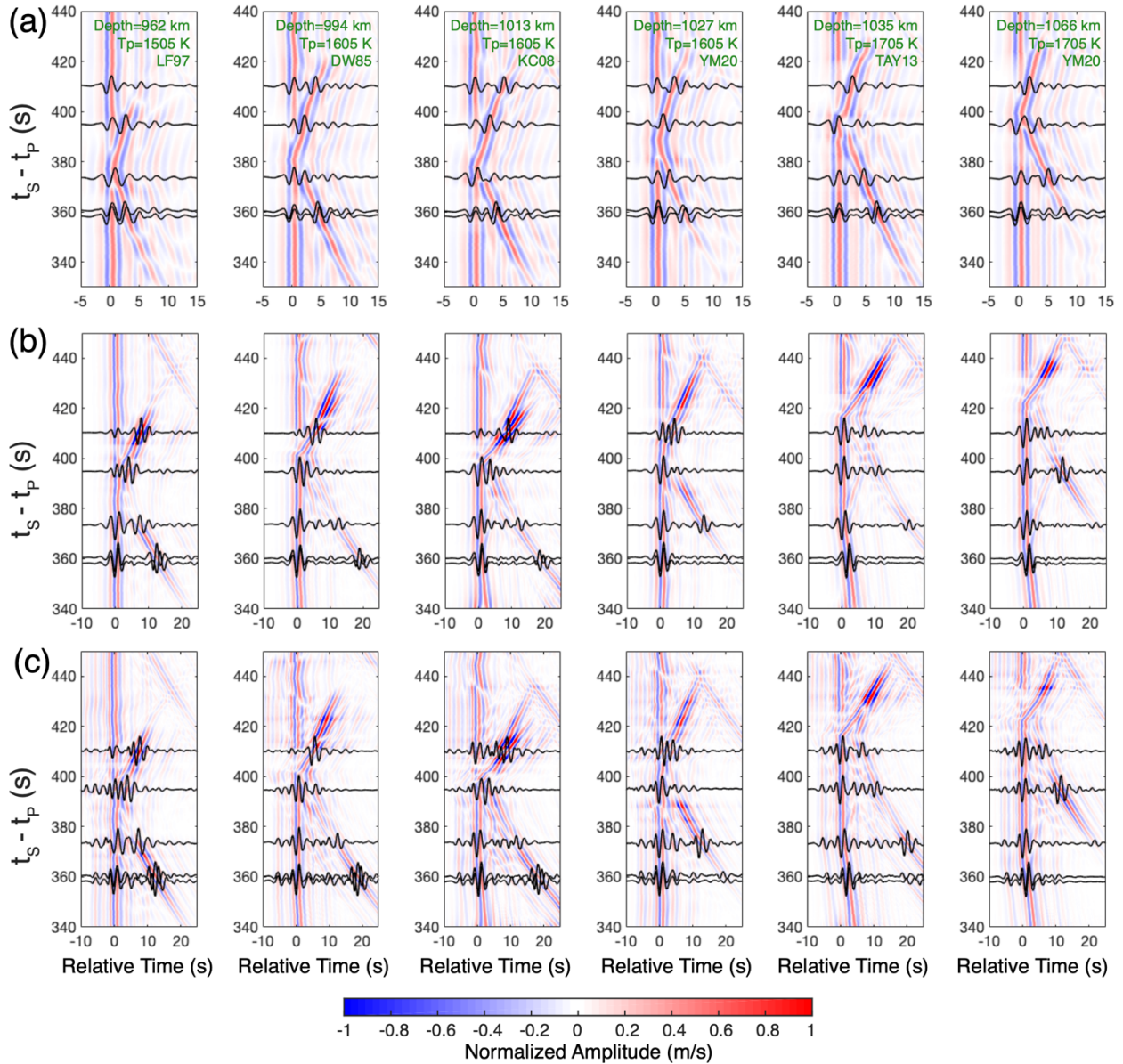
Fig. S1-14. Synthetic waveforms for (a) P triplication on the vertical component; and S triplication on the (b) transverse and (c) radial components. These synthetics are aligned on the first P- and S-arrivals and ordered by $t_S - t_P$. The '1000' depth increases from left to right. Black waveforms denote the synthetics with the same $t_S - t_P$ values as the five LF and BB events. Background color shows the synthetics across the entire distance range of triplications. Model parameters are shown in the top of panel (a): '1000' depth, mantle potential temperature (T_P) and composition models. The composition models include DW85 (4), KC08 (5), LF97 (6), TAY13 (7), YM20 (8).
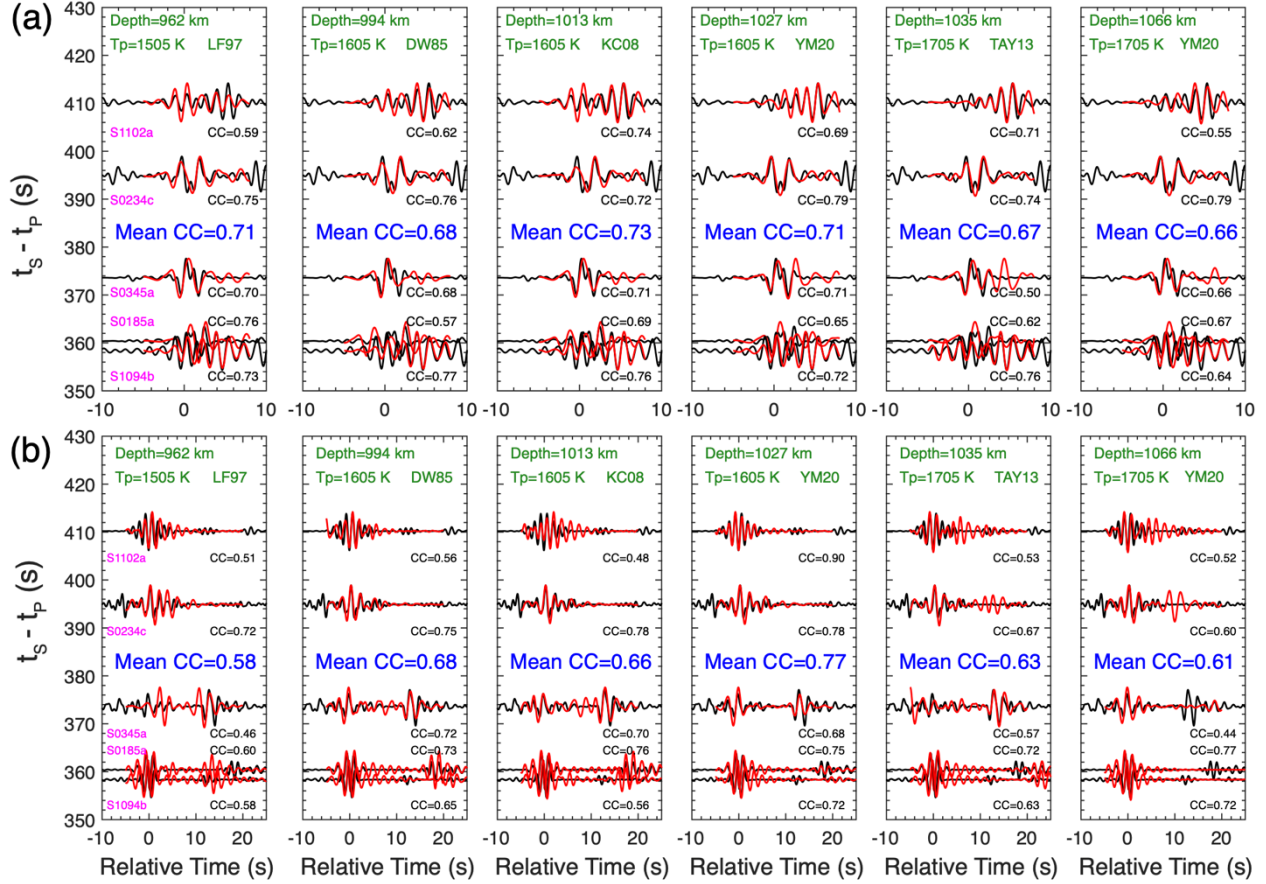
Fig. S1-15. Synthetic waveform modeling for (a) P triplications and (b) S triplications. Data are shown in black, and synthetics are shown in red. Correlation coefficients (CC) between synthetics and data are listed on the right. The mean CC for five events is shown in blue. Model parameters are shown in the top of each panel: '1000' depth, mantle potential temperature (T_P) and composition models. The composition models include DW85 (4), KC08 (5), LF97 (6), TAY13 (7), YM20 (8).

SI2. Supplementary Figures and Tables for Structure Models of Mars
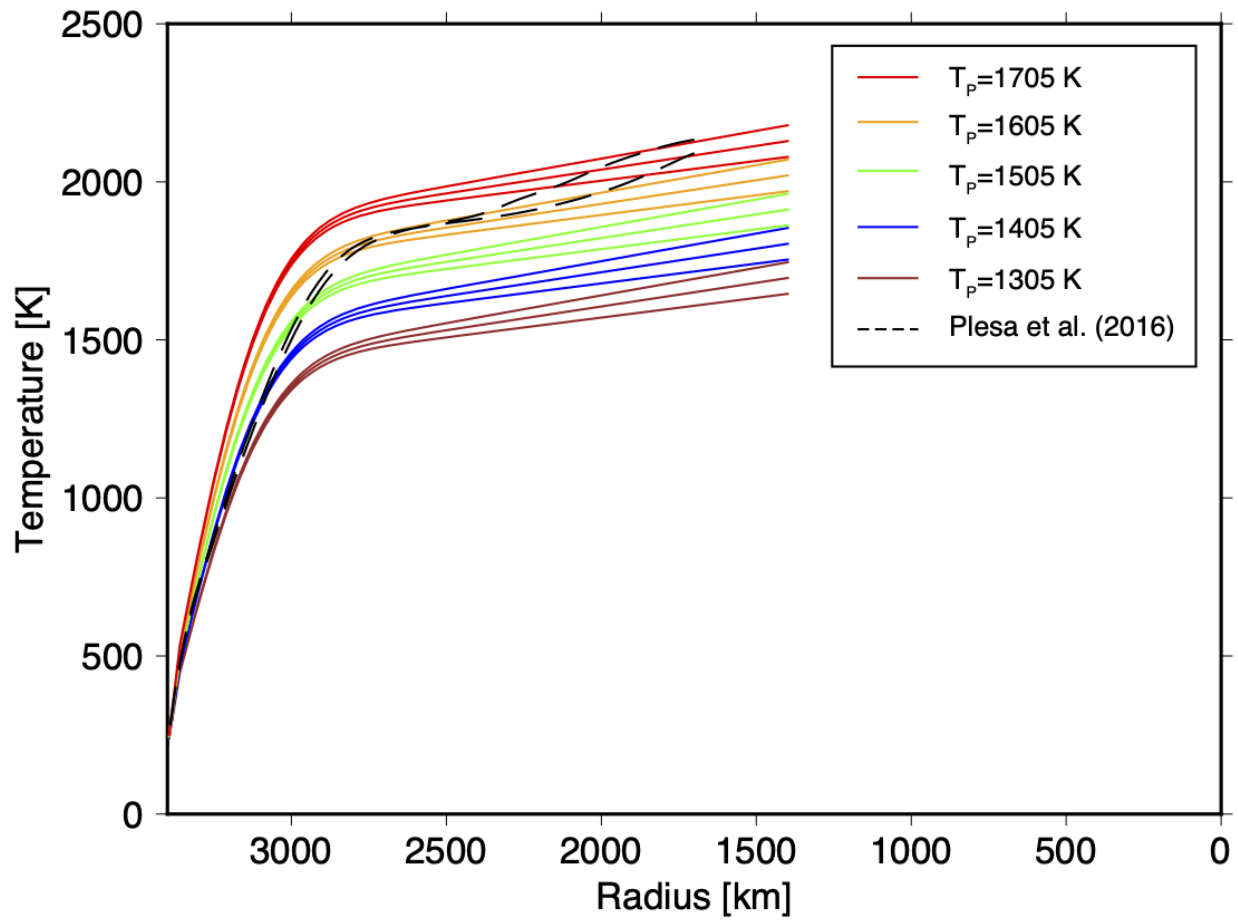
Fig. S2-1. Summary of areotherms (mantle temperature profiles) used in this study. The color represents the mantle potential temperatures (T_P). Three thermal gradients (0.125, 0.150, and 0.175 K/km) were used for each mantle potential temperature. The black dashed line denotes the areotherms from (9).

Table S2-1. Three-layer crust model beneath the InSight lander constrained from receiver functions (3).

Depth (km)	V_P (km/s)	V_S (km/s)
0.00	2.76	1.55
7.98	2.76	1.55
7.98	4.42	2.54
20.45	4.42	2.54
20.45	6.10	3.59
39.71	6.10	3.59
39.71	6.87	4.02
80.00	6.87	4.02

Table S2-2. Major element compositions of bulk silicate Mars (crust + mantle) in wt %.

Composition Models	SiO₂	Al₂O₃	MgO	MnO	CaO	Na₂O	K₂O	FeO
Dreibus and Wänke (1985)	44.40	3.02	30.20	0.46	2.45	0.50	0.037	17.90
Lodders and Fegley (1997)	45.49	2.89	29.71	0.37	2.35	0.98	0.110	17.22
Khan and Connolly (2008)	44.00	2.50	33.00	N/A	2.20	N/A	N/A	17.00
Taylor (2013)	43.70	3.04	30.50	0.44	2.43	0.53	0.037	18.10
Yoshizaki and McDonough (2020)	45.50	3.59	31.00	0.37	2.88	0.59	0.043	14.70
Sanloup (1999) (EH45:H55)	47.50	2.50	27.30	0.40	2.00	1.20	N/A	17.70

Fig. S2-2. Depth profiles of (a) density, (b) V_P and (c) V_S derived from the six composition models [DW85 (4), EH45 (10), KC08 (5), LF97 (6), TAY13 (7), YM20 (8)] and the areotherms described in Fig. S2-1.

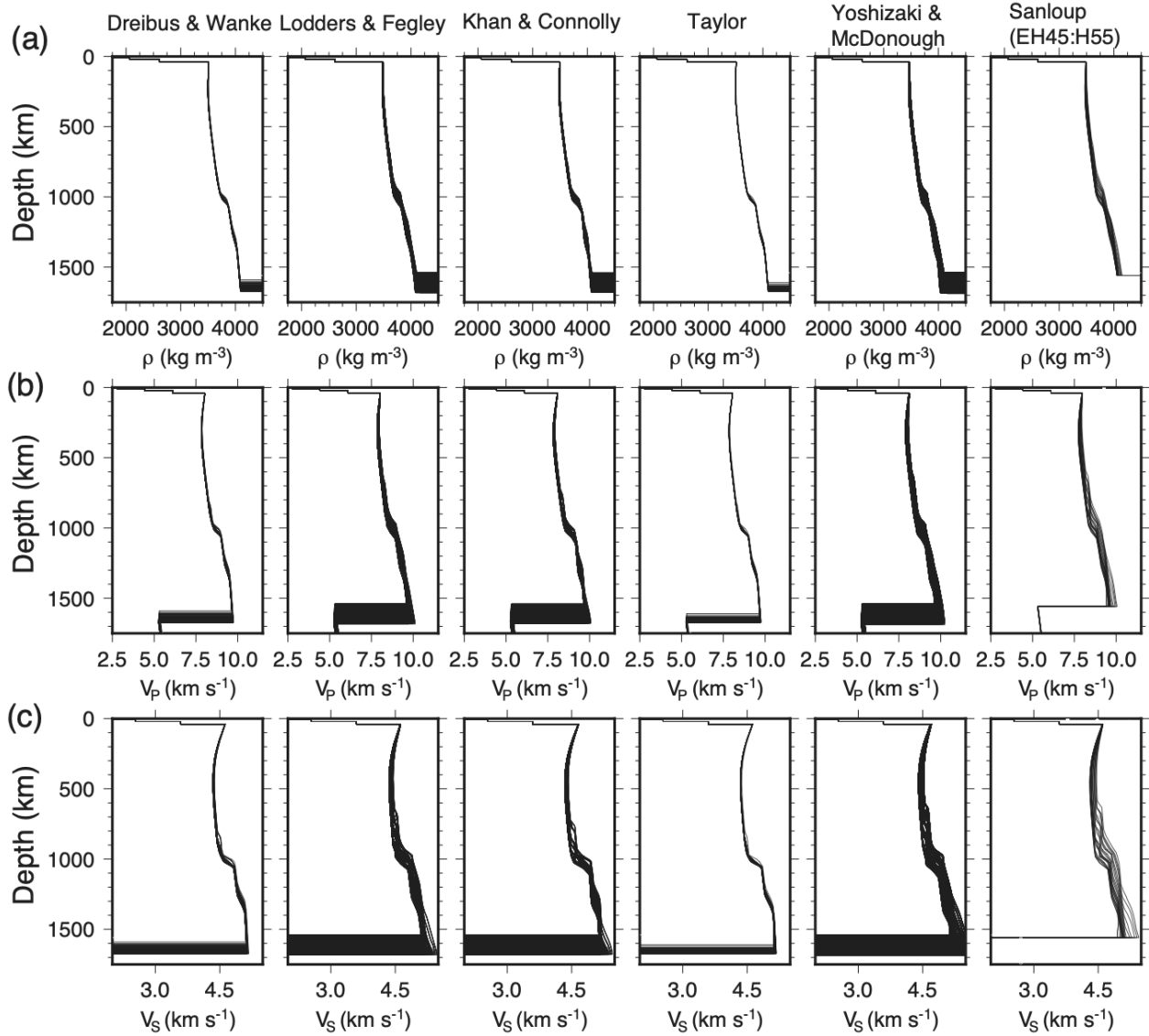# SI3. Supplementary Figures and Tables for Geodynamic Modeling of Thermochemical Evolution of Mars
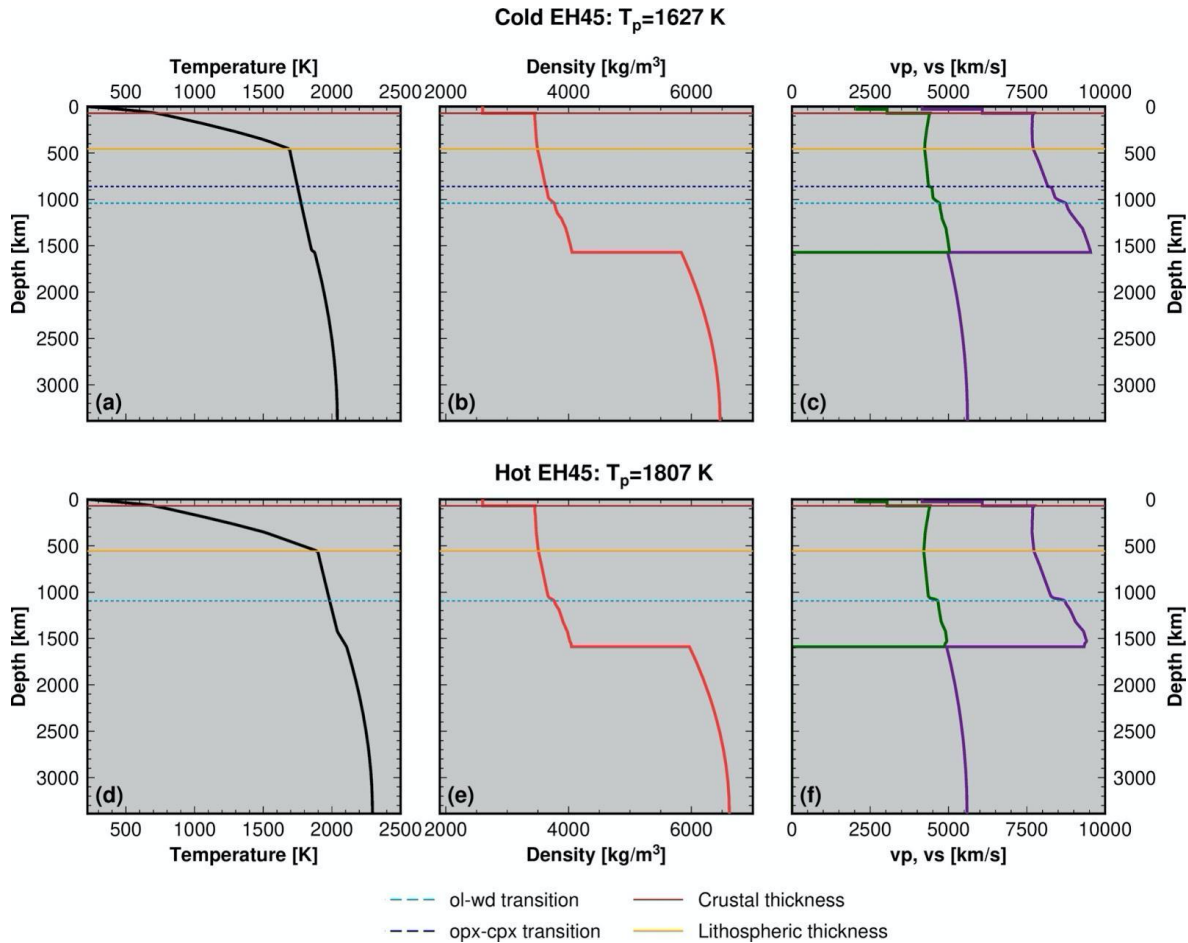
Fig. S3-1. Illustration of the sensitivity of the phase transition to the present-day thermal structure. Two distinct thermo-chemical evolutions are considered. Top: a combination of mantle rheology (η_0=3 10^{20} Pa s, E^*=420 kJ/mol, V^*=1 cm^3/mol) and initial thermal state (Tm_0=1715 K, Tc_0=1935 K) leading to a relatively cold mantle at present-day with a potential temperature Tp=1627 K. Bottom: a combination of mantle rheology (η_0=10^{22} Pa s, E^*=200 kJ/mol, V^*=5 cm^3/mol) and initial thermal state (Tm_0=1700 K, Tc_0=2100 K) leading to a relatively hot mantle at present-day with a potential temperature Tp=1807 K. Both models share the same EH45 bulk composition and the same core size (Rc=1800 km). The three columns display the present-day temperature (a,b), density (b,e) and seismic velocity (c,f) profiles. The crustal and lithospheric thicknesses (displayed in brown and yellow, respectively) are different for the cold and hot models because they result from a different thermo-chemical history. The resulting distinct thermal structure allows for the occurrence of both deep post-olivine transition (whose depth is depicted by the dashed light blue lines) and shallow orthopyroxene-to-clinopyroxene transition (dark blue dashed lines) for the cold thermal structure. In contrast, the evolution that yields a hot mantle only allows for the occurrence of the deep post-olivine transition.

EH45 composition   □ n=338   ■ n=224
(a) (b) (c) (d)

TAY13 composition   □ n=8   ■ n=0
(e) (f) (g) (h)

YM20 composition   □ n=805   ■ n=0
(i) (j) (k) (l)

LF97 composition   □ n=3   ■ n=0
(m) (n) (o) (p)

KC08 composition   □ n=90   ■ n=26
(q) (r) (s) (t)

Axis labels: Heat flux [mW/m^2]; Crustal enrichment, Λ; D_{ol-wd} [km]; $D_{opx-cpx}$ [km]; Log$_{10}$(1+count)
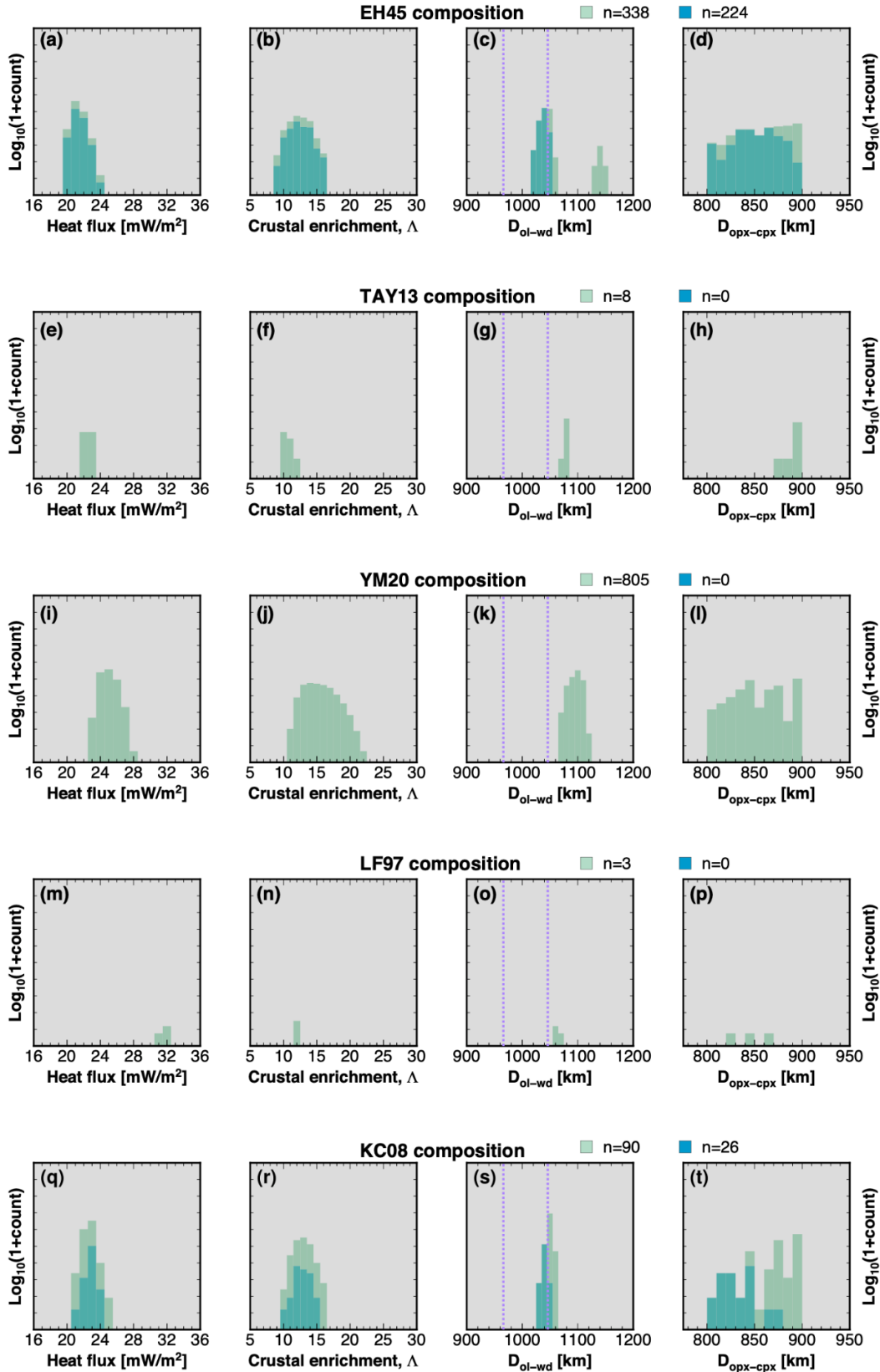
□ Possible evolutions compatible with present day crustal thickness D_{cr}=39–72 km and a lithospheric thickness > 500 km

■ Evolutions compatible with at least the post-olivine transition depth D_{ol-wd}=1006±40 km

26

Fig. S3-2. Results of the exploration of the parameter space for the modeling of Mars' thermo-chemical evolution. Histograms of the model space compatible with a present-day crustal thickness ranging between 39 and 72 km and lithosphere thicker than 500 km (light blue), the evolutions that, in addition to crustal and lithospheric thickness requirements, are compatible with the occurrence of post-olivine transition at a depth range of *Dol-wd*=1006±40 km (medium blue). Each row corresponds to the bulk compositions listed in Table 3-2. The model space (Table S3-1) is sampled 10^5 times per composition using random uniform distributions. The corresponding numbers of thermo-chemical histories that satisfy the requirement for each of the three subsets are indicated. The vertical dotted lines represent the minimum and maximum ranges for *Dol-wd* inferred by seismic data.

Table S3-1. Ranges considered for the values of the governing parameters for the modeling of Mars' thermo-chemical evolution.

Parameter	Range
Initial uppermost mantle temperature, Tm_0	1700-2000 K
Initial core-mantle boundary temperature, Tc_0	Tm_0 + 100-500 K
Crustal enrichment factor, Λ	5-30
Mantle reference viscosity, η_0	10^{20}-10^{23} Pa s
Mantle effective activation energy, E^*	100-500 kJ/mol
Mantle effective activation volume, V^*	0-10 cm^3/mol
Core radius, Rc	1750-1950 km

Table S3-2. Bulk concentrations of Heat-Producing Elements for the four Martian compositions considered. Note that since KC08 does not assume a specific HPE content, we considered the same values as in TAY13.

Composition \ heat-producing elements content	U [ppb]	Th [ppb]	K [ppm]
EH45 (10)	14	54	284
TAY13 (7)	16	56	305
LF97 (6)	16	55	920
YM20 (8)	18	68	360
KC08 (5)	16	56	305

Table S3-3: Characteristics (min-max and 1-σ ranges) associated with the EH45 evolutions compatible with the post-olivine transition constraints (*Dol-wd*=1006±40km).

Characteristics	Min-Max range	1-σ range
Tm₀ [K]	1700-1938	1788±54
Λ	10-16	13±2
η_0 [Pa s]	$10^{20.1}$-$10^{22.2}$	$10^{21.2\pm0.5}$
E* [kJ/mol]	101-499	318±112
V* [cm^3/mol]	0-9.53	5.1±2.6
Present-day surface flux [mW/m^2]	20-24	21±0.7
Present-day *Tp* [K]	1556-1673	1621±26
Present-day *Dcr* [km]	51-72	63±5

Table S3-4: Characteristics (min-max and 1-σ ranges) associated with the KC08 evolutions compatible with the post-olivine transition constraints (*Dol-wd*=1006±40km).

Characteristics	Min-Max range	1-σ range
Tm$_0$ [K]	1704-1957	1789±70
Λ	10-15	13±1
η_0 [Pa s]	$10^{20.4}$-$10^{21.6}$	$10^{20.9\pm0.5}$
E* [kJ/mol]	102-386	238±87
V* [cm^3/mol]	0.5-7.6	5.0±2.2
Present-day surface flux [mW/m^2]	21-24	23±0.5
Present-day *Tp* [K]	1486-1539	1516±15
Present-day *Dcr* [km]	56-71	67±4

SI4. Synthetic Tests and Detectability of Mantle Triplications

4.1 Influence of Focal Mechanisms on Triplicated Waveforms

To investigate the influence of focal mechanisms on the waveform modeling results, we generated 64 arbitrary sources by changing the strike, dip, and rake values of the fault. The strike ranges from 0 to 180 deg with a 60-deg step size, and the dip and rake range from 0 to 90 deg with a 30-deg step size. We used the best-fitting model with the lowest P-misfit in Fig. 3A ($T_P = 1605\ K$, KC08) as an example and computed synthetics with these 64 sources. First, we selected three types of sources to compare the waveform differences: 1) normal fault (Fig. S4-1a), 2) strike slip (Fig. S4-1b) and 3) reverse fault (Fig. S4-1c) in the synthetic tests. The normal fault source here is the same as the one shown in Fig. S1-13 which was used for the synthetic waveform modeling. The polarities of P and S triplications vary depending upon the radiation patterns, whereas the travel-times remain the same (Fig. S4-1d, e). The amplitudes of crustal phases on the vertical and radial components also differ among these models as a result of various sources (Fig. S4-1d, e).

Next, we compare the waveforms from all 64 arbitrary sources. We adjusted the waveforms to the same polarities and then quantified the amplitude changes of the triplications as a function of the sources. We compared the waveforms in these two time-windows: 1) -5 to 15 s for P triplication and 2) -10 to 30 s for S triplication. P triplications display very small amplitude changes (5-25%) due to the source variations (Fig. S4-2a). Most amplitude variations are caused by the crustal phases which are more sensitive to different focal mechanisms. Similarly, S triplications also show <25% amplitude change for most distances, even though a small range of distances can have up to 40% amplitude changes (Fig. S4-2b, c). All these waveforms show mean CC greater than 0.7 at the same distance. This suggests that the triplicated waveforms are not very sensitive

to focal mechanisms mainly due to their similar take-off angles as the first P- and S-arrivals. Since we do not have any constraint on the focal mechanisms of the five events used in this study, we cannot choose different sources for each event but to assume a constant source for all events for simplicity. This synthetic test supports that our waveform modeling results are most likely independent from the choice of sources.
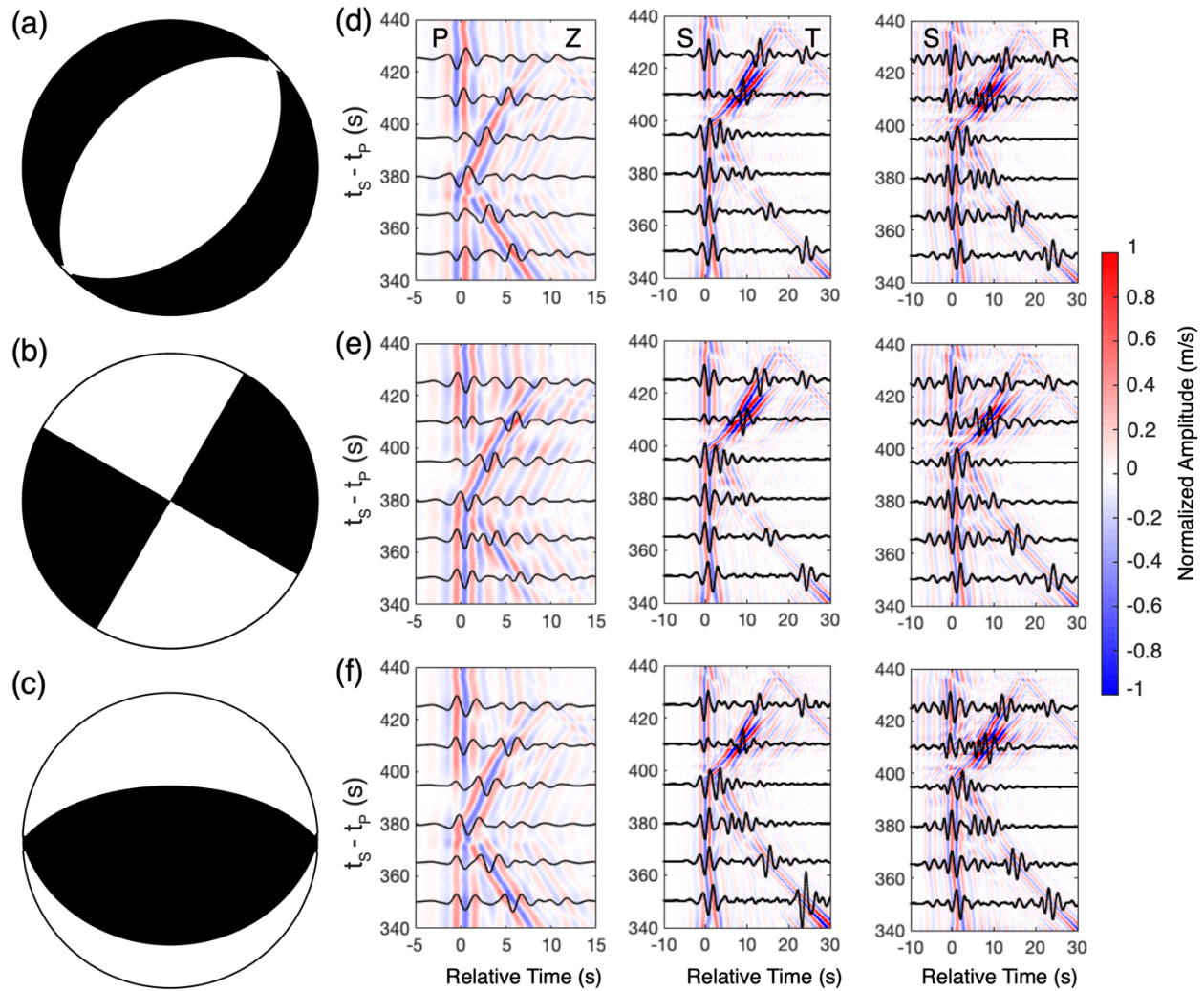
Fig. S4-1. Effects of focal mechanisms on P and S triplicated waveforms. Three types of sources are shown as an example in the synthetic tests: (a) normal fault, (b) strike slip and (c) reverse fault. The corresponding synthetic waveforms are shown in (d), (e) and (f) respectively. From left to right in each panel are P triplications on the vertical component (Z), S triplications on the transverse component (T) and radial component (R). Background colors display the synthetics across the entire distance range. The black curves highlight the synthetic waveforms at certain distances.

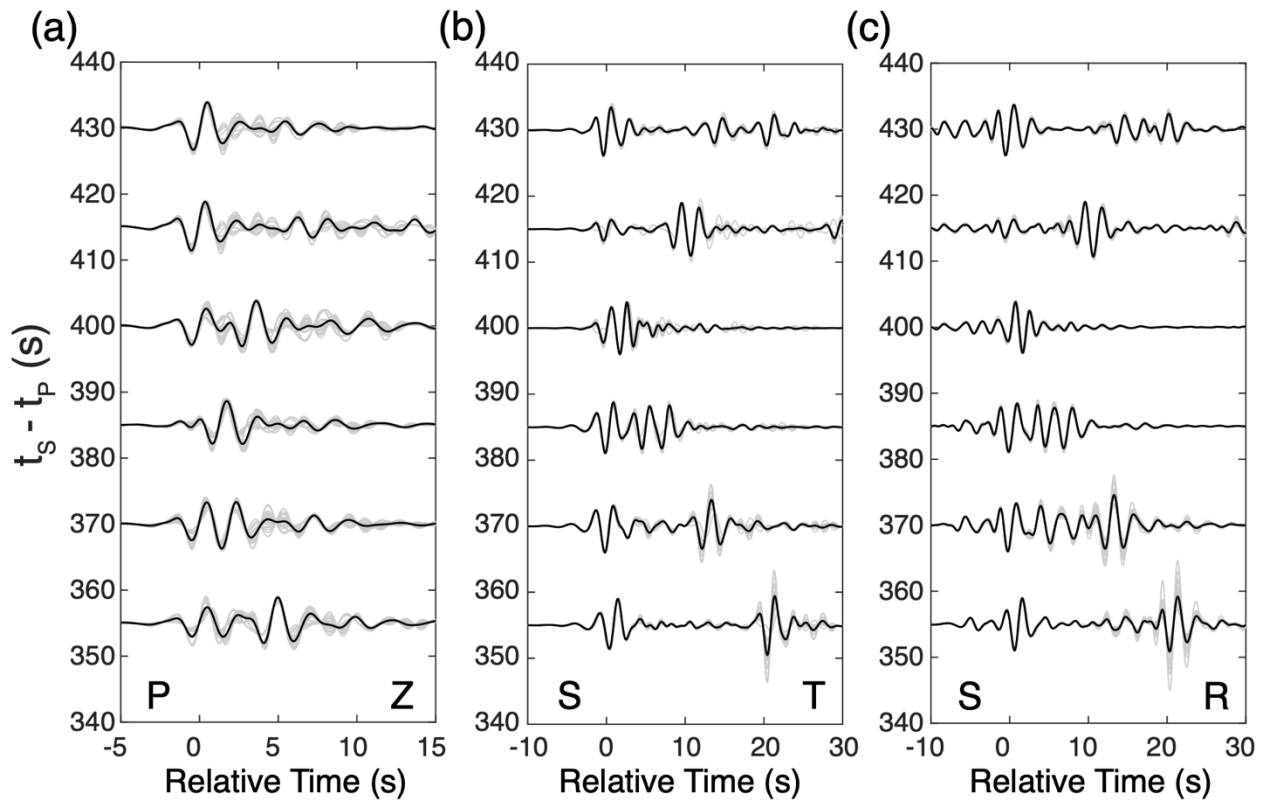**Fig. S4-2.** Comparisons of P- and S-waveforms from 64 arbitrary sources. (a) P triplication on the vertical component (Z), (b) S triplication on the transverse component (T) and (c) radial component (R). The gray lines show the individual seismograms from different sources. The black lines represent the mean amplitudes of these seismograms.

4.2 Sharpness of the 1000-km Discontinuity

In addition to the '1000' depth, the sharpness of the post-olivine transition (i.e., phase transition thickness) can provide additional constraints on the temperature and composition of Martian mantle. High pressure phase equilibrium experiments, calculations, and derived models demonstrate that the compositional enrichment of iron (11–14) and water content (15–18), as well as a lower mantle temperature (17, 19) can broaden the thickness of phase transition (see SI 5.1 for more details). Here, we define the discontinuity thickness as H. Note that H could be different from the phase transition thickness because the relationships between these two parameters could become non-linear when most phase transitions only occur within a small width of the phase loop (13, 20). We fixed the '1000' depth (1027 km) in the best-fitting model shown in Fig. 3B ($T_P =$ 1605 K, YM20) and varied H from 0-200 km with a 10 km interval (Fig. S4-3a, b). The H value in the best-fitting model is 84.5 km. We computed the travel-time curves of P and S triplications using two end-member models (H=0 and H=200 km) and one intermediate model (H=100 km). As the '1000' discontinuity becomes sharper (i.e., decreasing H), the triplications extend to a wider distance range, and the travel-times of DE branches are delayed (Fig. S4-3c, d). We computed synthetic waveforms using these models with various H values. We used the same method as described in the Methods section of "Synthetic Waveform Modeling" to compute these synthetics, as well as the misfits between data and synthetics. Our goal is to constrain the discontinuity thickness (H) based on the waveform modeling.

The waveform modeling results for P and S triplications are shown in Fig. S4-4a and Fig. S4-4b respectively. We show the misfits of P and S triplications as a function of H in Fig. S4-5. The P triplication is not very sensitive to the sharpness of '1000' discontinuity because the misfits change very little when H is smaller than 120 km. On the contrary, the misfits of S triplications

are minimized when H=60 km. S triplications are more sensitive to H because the distances of S0185a and S1094b events are close to the lower edge of S triplication (Fig. S4-4b). However, these events are all concentrated near the center of P triplication (Fig. S4-4a), thus reducing their sensitivity to H. We further compute the total misfits of both triplications which are also minimized when H=60 km. As shown in Fig. S4-4b, the synthetic S triplications disappear in S1094b and S0185a as H increases from 60 to 100 km. The total misfit also approaches its maximum value when H is greater than 100 km (Fig. S4-5). This suggests that the upper bound of phase transition thickness is close to 100 km. We also observe that the amplitudes of synthetic S triplications become much larger than the data in S1094b and S0185a as H decreases from 60 to 20 km (Fig. S4-4b). This leads to the increase of total misfit. Furthermore, the total misfit increases sharply when H is decreased from 20 to 10 km (Fig. S4-5). Therefore, we constrain the lower bound of the phase transition interval to be 20 km. This lower bound is also consistent with the minimum phase transition thickness predicted from mineral physics (Fig. 4b). In summary, based on waveform modeling, we constrain the discontinuity thickness to be 60 ± 40 km, corresponding to a pressure increase of 0.76 ± 0.51 GPa. This is a more gradual phase transition compared to the sharp 410-km discontinuity observed on Earth [H<10km or 0.4 GPa, e.g., (21)]. It can be most easily explained by the higher iron content in the Martian mantle, but a higher water content could also play a role.
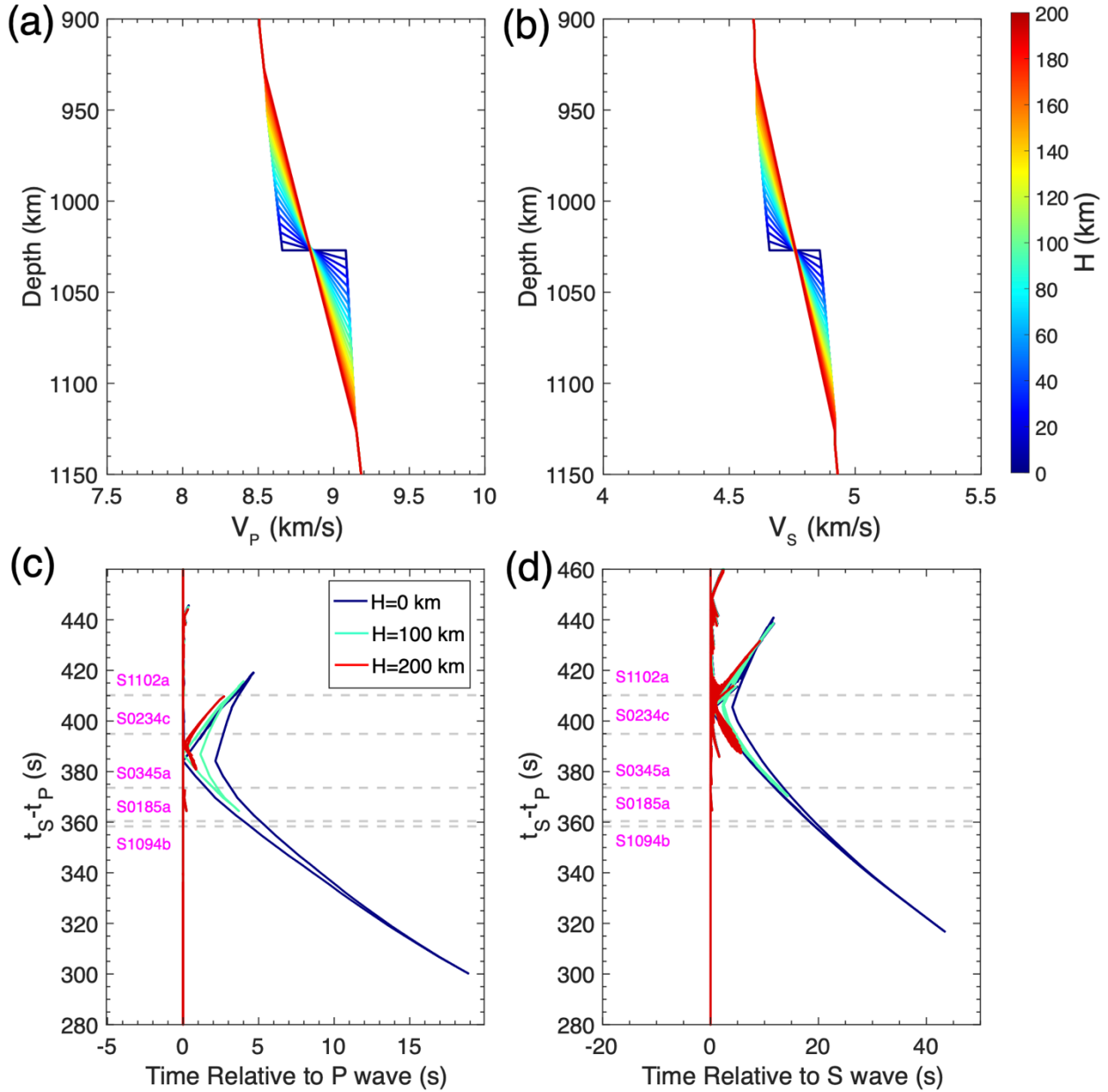
Fig. S4-3. Modeling of the sharpness of post-olivine transition. (a) V_P and (b) V_S profiles of models with the discontinuity thickness (H) between 0-200 km. The '1000' depth is fixed at 1027 km which is the same as the best-fitting model shown in Fig. 3B. Travel-time curves of (c) P triplication and (d) S triplication for the models with H=0, 100 and 200 km. The grey dashed lines highlight the S−P times of the five events used in this study.
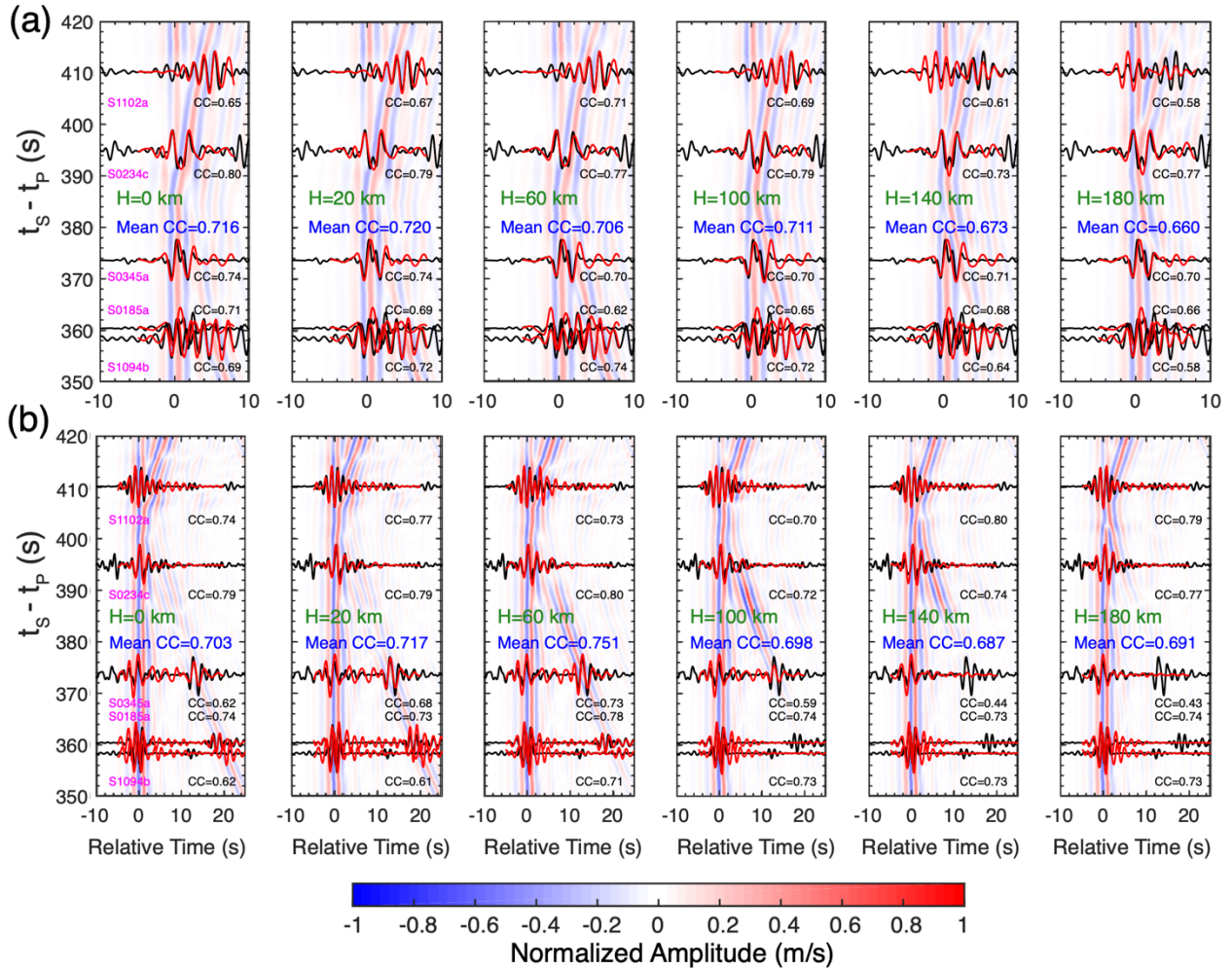
Fig. S4-4. Synthetic waveform modeling of (a) P and (b) S triplications by using models with a range of discontinuity thickness (0-200 km). Data are shown in black, and synthetics are shown in red. Correlation coefficients (CC) between the synthetics and data are listed on the right. Mean CC of five events are shown in blue. The discontinuity thickness (H) is shown in green. The background color represents the amplitudes of synthetics.

Fig. S4-5. Misfits of P and S triplications as a function of discontinuity thickness (H). The red and blue dashed lines represent the misfits of P and S triplications, respectively. The black solid line denotes the total misfit.

4.3 Depth of the opx to HP-cpx Phase Transition
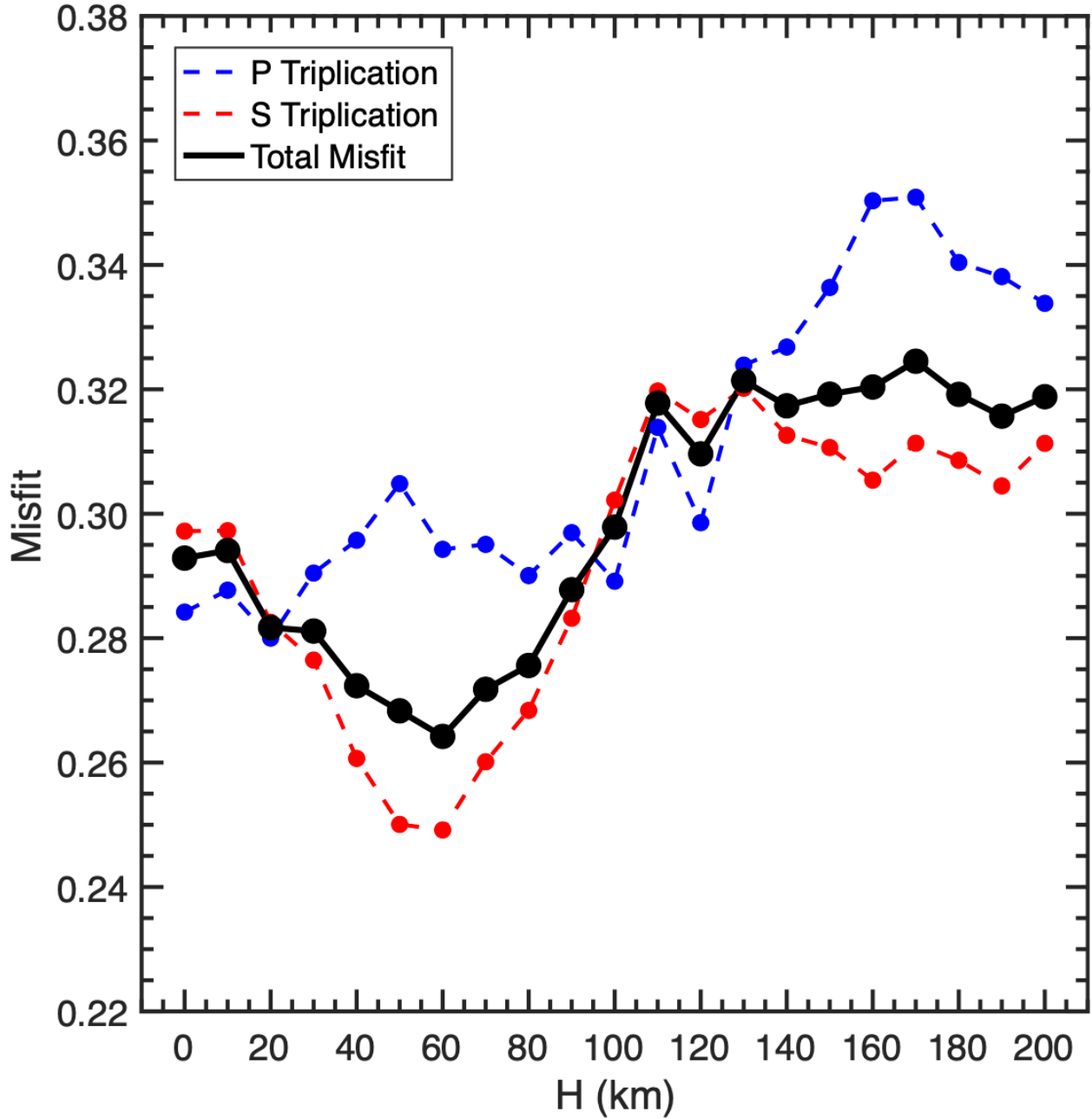
The two triplications caused by opx to HP-cpx (Branch A-C) and post-olivine transitions (Branch D-F) closely intersect with each other (Fig. 1). Therefore, it was difficult to distinguish these two triplications in the data and synthetics (Fig. 2). Here, we performed a synthetic test to investigate if the opx to HP-cpx phase transition exists above the MTZ and quantify its depth if present. We used the best-fitting model shown in Fig. 3B and removed the '800' discontinuity associated with the opx to HP-cpx phase transition, while keeping the upper mantle and MTZ structures the same (Fig S4-6a, c). We computed the synthetics using the models with and without the '800' discontinuity. We then computed the misfits between data and synthetics using the method described in the Methods section of "Synthetic Waveform Modeling". We find that the misfit of P triplication increases from 0.29 to 0.30 (Fig. S4-6b), and the misfit of S triplication increases from 0.23 to 0.24 (Fig. S4-6d) after removing the opx to HP-cpx phase transition. However, given the small differences in waveform misfits, additional seismic data are needed to definitively argue for or against the existence of the '800' discontinuity in Mars.

Even though we cannot definitively detect the '800' discontinuity, we can still predict its depth based on our constraints on the '1000' depth and insights from mineral physics. Over the range of bulk compositions considered, the thermodynamic formulation and dataset of (22) estimate that the post-olivine and opx to HP-cpx transitions should have Clapeyron slopes of about 2.7 MPa/K and 8.4 MPa/K, respectively. The positive Clapeyron slopes indicate that the depths of these two discontinuities both increase with temperature (Fig. S4-7a, b). Therefore, the depths of these two discontinuities are positively correlated (Fig. S4-7c). The opx to HP-cpx phase transition is more sensitive to temperature and increases from 600 to 1000 km depth over the temperature range of our models, because its Clapeyron slope is ~3 times larger than that of post-olivine transition.

Similarly to Fig. 3, we plot the misfits of P and S triplications as a function of opx to HP-cpx depth. Note that the post-olivine transition is the primary contributor to the misfits of triplications. We used the same misfit thresholds as described in the main text to select the low-misfit models. The depth of opx to HP-cpx is predicted to be $780 \pm 169\ km$ (Fig. S4-7d) and $854 \pm 120\ km$ (Fig. S4-7e) based on the P and S triplications, respectively. These two depths agree within the uncertainty range. Finally, we computed the total misfits (Fig. S4-7f) from which we can predict the depth of opx to HP-cpx to be $850 \pm 116\ km$. We note that this depth range is not directly constrained from the seismic data but rather predicted from the correlation between the depths of post-olivine and opx to HP-cpx transitions based on mineral physics.
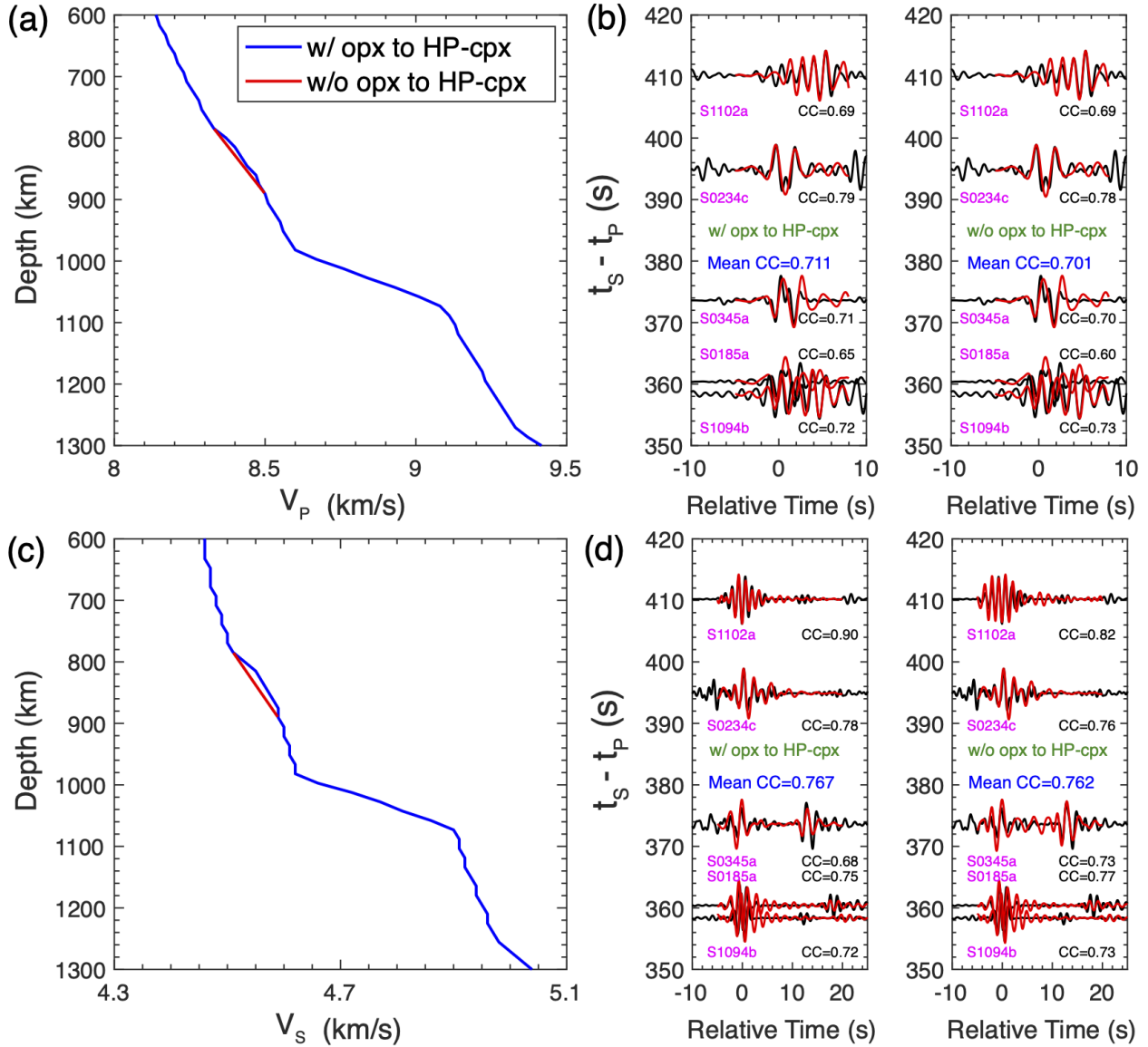
Fig. S4-6. Synthetic tests to validate the existence of opx to HP-cpx phase transition. The (a) V_P and (b) V_S profiles of the models with (blue) and without (red) the opx to HP-cpx phase transition. The blue model is the best-fitting model shown in Fig. 3B. Synthetic waveform modeling of (c) P and (d) S triplications by using the models with and without the opx to HP-cpx phase transition. Data are shown in black, and synthetics are shown in red. Correlation coefficients (CC) between the synthetics and data are listed on the right. Mean CC of five events are shown in blue.
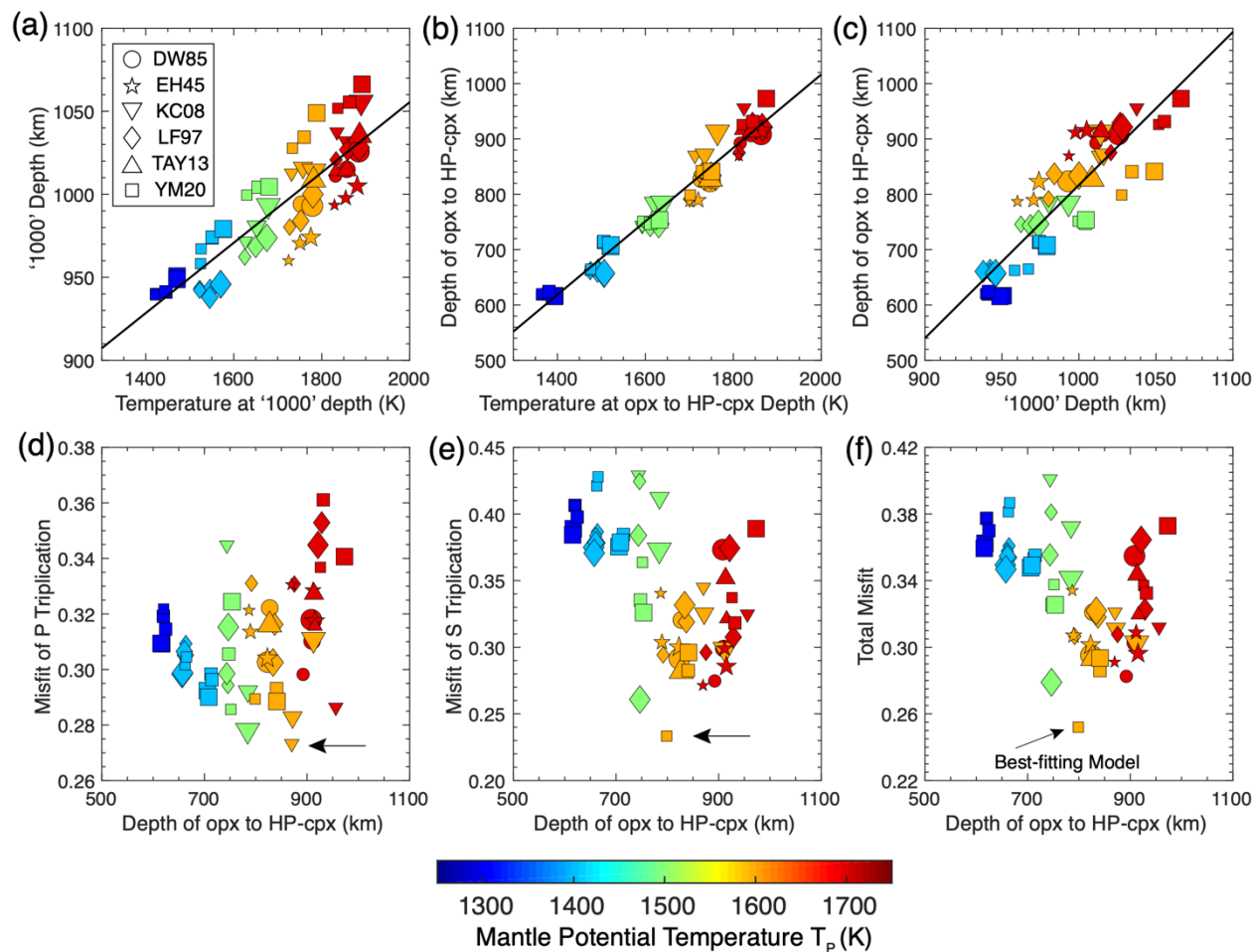
Fig. S4-7. Depth of opx to HP-cpx phase transition inferred from the correlations with the '1000' depth. (a) '1000' depth and (b) opx to HP-cpx depth shown as a function of temperature. (c) '1000' depth vs. depth of opx to HP-cpx. The black lines are the best linear fitting to the correlations. Misfits of (d) P triplication, (e) S triplication and total misfit shown as a function of opx to HP-cpx depth. The legends are the same as Fig. 3. Color represents the mantle potential temperature. Black arrows highlight the best-fitting models shown in Fig. 3.

4.4 Detectability of P and S Triplications

We used AxiSEM synthetics to investigate the detectability of mantle triplications on Mars. The detectability study required the knowledge of noise levels on Martian surfaces. SEIS is covered by the Wind and Thermal Shield (WTS) to provide protection from wind and thermal variations on Mars (23). However, due to the ground coupling between atmosphere and InSight Lander/WTS, multiple sources of noise can still contribute to SEIS data such as the environmental noise from atmospheric pressure change or wind, and instrument self-noise (24). We used the mean noise amplitude spectra from the VBB data in July 2019 (25) to study the characteristics of Martian noise. Fig. S4-8 illustrates the comparison between Martian and terrestrial noise (26) in velocity. The Martian noise level is significantly lower than Earth, especially between 1-10 s period. On Earth, part of the micro-seismic noises originating from ocean waves dominate the 1-10 s period range (27). Martian noise is even lower than the New Low Noise Model (NLNM) on Earth due to the lack of oceans on the surface. The extremely quiet environment on Mars provides an ideal condition to detect subtle seismic signals.

Martian noise shows strong diurnal variations: the daytime noise level is ~10 times stronger than the nighttime noise level (Fig. S4-8). The diurnal difference is due to the more turbulent atmospheric activities during the day (24, 28). At the beginning of the mission, the nighttime was initially the ideal time to detect seismic events due to the low noise level. However, after one-Earth year (six Mars months) of noise evolution, the nighttime noise level increased and converged with daytime noise in June 2020, which reduced the number of detectable seismic events. In early 2021, the night noise level started to decrease again increasing the chances for new events to be detected. The second feature is that the horizontal components (BHN and BHE) are noisier than the vertical component (BHZ) in long period range (> 5s). We used the nighttime noise level as the noise floor

44

to determine the detectability of triplications. We computed the average amplitude spectrum between BHE and BHN components as horizontal noise level for S-wave detections. The vertical (BHZ) amplitude spectrum was used for P-wave detections.

We used synthetic waveforms of P triplications computed from the EH45TcoldCrust1 model (29) to investigate the energy partitioning at triplication distances. We used the same source as shown in Fig. S1-13 and increased the dominant frequency to 1 Hz. Unlike in the Methods section of "Synthetic Waveform Modeling", here we turned on crustal and mantle attenuation using the attenuation profiles scaled from the Preliminary Reference Earth Model (30). In Fig. S4-9a, two triplication patterns are evident in the modeled waveforms, with arrival times consistent with the predicted travel-time curves from TauP (31). The earlier triplication matches the ray-theory predictions for the structure associated with the '800' discontinuity (opx to HP-cpx), whereas the later one is from the '1000' discontinuity (post-olivine transition). In both cases, the synthetics show that the amplitudes of the triplicated arrivals are comparable or even larger than that of the first P arrivals. For the P-triplications, the travel-times of the prograde and retrograde branches are only ~5 seconds later than first P arrivals. Our synthetics reveal that high frequency waves (1 Hz in Fig. S4-9a) are required to distinguish each branch, at lower frequencies the triplication is expressed as a broadening of the P-waveform at the triplication distance. Furthermore, the modeling reveals that the P triplications are followed by crustal reverberations such as Pv85pP which do not interfere with the P triplications.

To determine the detectability of triplications for marsquakes, we cut a 15-s time window centered around the triplication at 72 degrees and calculated the amplitude spectrum for comparisons with the VBB BHZ noise level (Fig. S4-9b). The magnitude thresholds are defined as the minimum magnitudes of events when the signals are ~10dB above the noise level. The

magnitude thresholds required for detections are Mw 2.5 and Mw 3.5 respectively using the night and day noise levels, which are comparable to the sizes of marsquakes (Mw 2.6-4.0) observed by SEIS (32, 33). We computed the SNR of P waves across different distances and frequencies from the difference between the amplitude spectra and BHZ night noise level (Fig. S4-9c). As the magnitude increases, the SNR will similarly increase and also result in a broader bandwidth above the noise (>10dB to be detectable). The period range for the detection of P triplications is between 1-15s, and distance range is between 60-75 degrees.

The synthetic waveforms of S triplications are more complicated with two triplications more closely intersecting with each other (Fig. S4-10a). The travel-times of S triplications are 10-15s later than the first S-waves, allowing them to be separable even in lower-frequency records. This will increase the chance of detecting the triplication since many high-quality events from InSight are low-frequency events (34). The S triplications are also followed by crustal reverberations and depth phases, which can be distinguished by their different moveouts. Similar to P waves, we cut a 50-s time window centered around the triplication at 70 degrees to calculate the amplitude spectra (Fig. S4-10b). The magnitude thresholds required for detections are Mw 3.5 and Mw 4.0 respectively using BHE/BHN night and day noise levels. The thresholds are larger than P waves because the horizontal components are noisier and S-wave attenuation is stronger in the EH45TcoldCrust1 model. Nonetheless, the magnitude thresholds are still comparable to the event sizes observed by SEIS (Mw 2.6-4.0) (32, 33). Fig. S4-10c illustrates the SNR of S triplications for different magnitudes of events. The period range for detection is between 1-25s and the distance range is between 60-85 degrees.
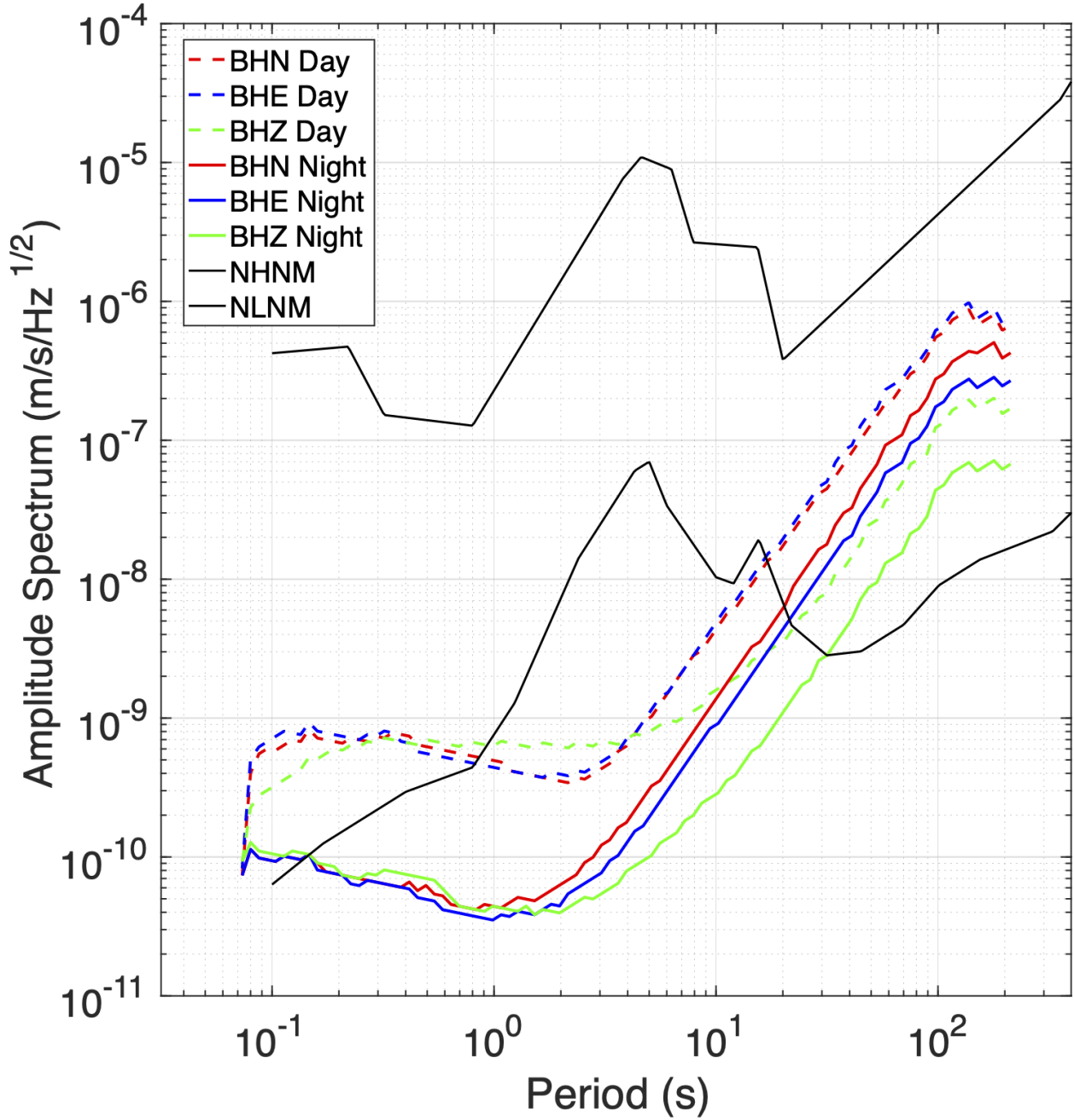
Fig. S4-8. Amplitude spectra of SEIS-VBB noise in velocity. The amplitude spectra are computed from the continuous VBB data in July 2019 (25). The dashed lines denote the day noise level, and the solid lines represent the night noise level. The Earth's noise spectra including New Low Noise Model (NLNM) and New High Noise Model (NHNM) are shown in black lines for comparison (26). The night noise level is used to calculate the magnitude thresholds for detecting P and S triplications.

Fig. S4-9. Detectability of P triplication. (a) Synthetic waveforms of P triplications on the vertical component using EH45TcoldCrust1 model (29). The red lines are the predicted travel-time curves from TauP (31). The synthetics are bandpass filtered between 1 and 100 s. (b) The amplitude spectra of P triplications for different event magnitudes. The amplitude spectra are computed from a 15 s time window centered around the triplication at 72 degrees. The VBB BHZ noise levels are shown by the black curves. (c) SNR of P triplications for different event magnitudes. The magnitude threshold is Mw=2.5. The period range is 1-15 s, and the distance range is 60-75 degrees to detect the P triplications.
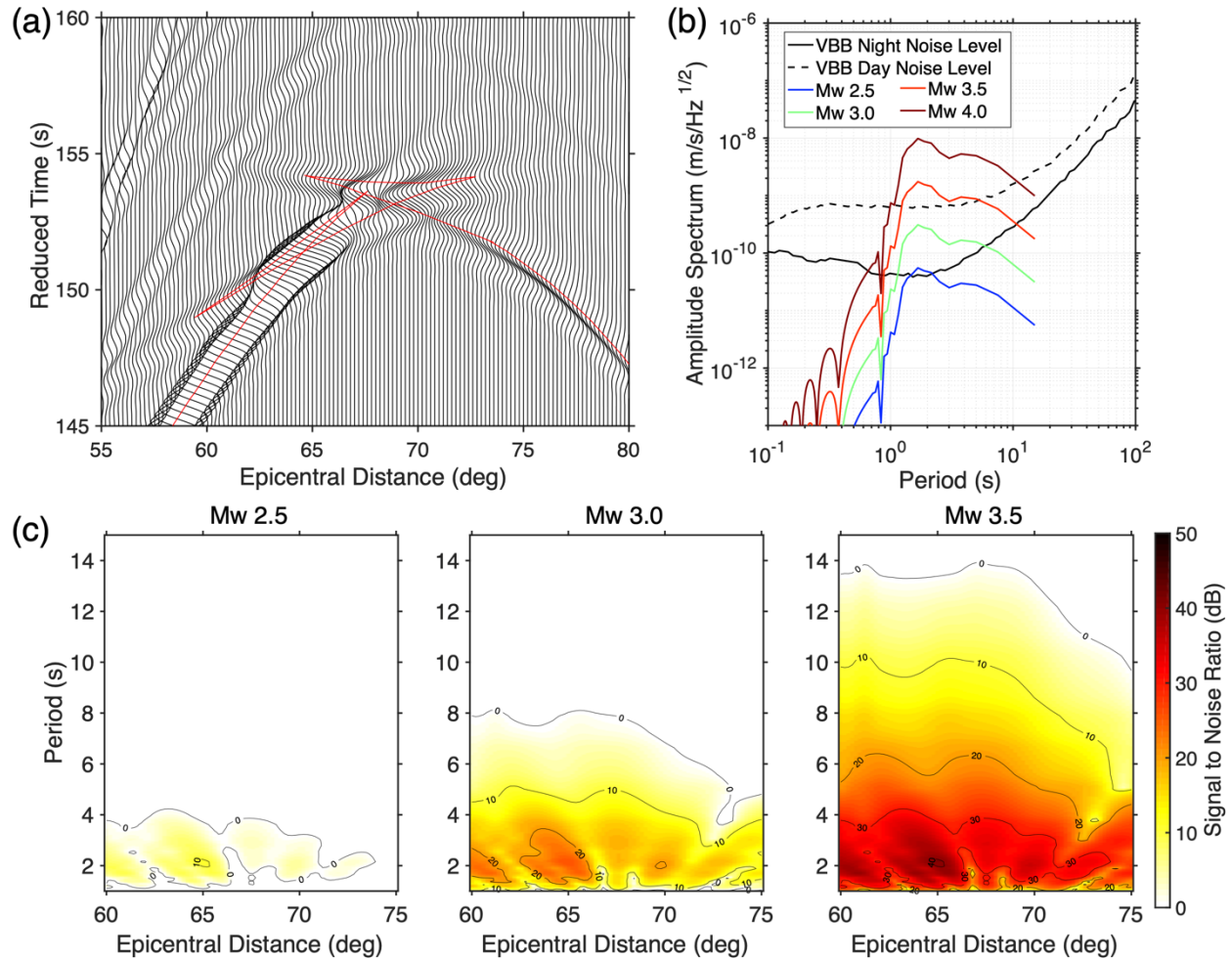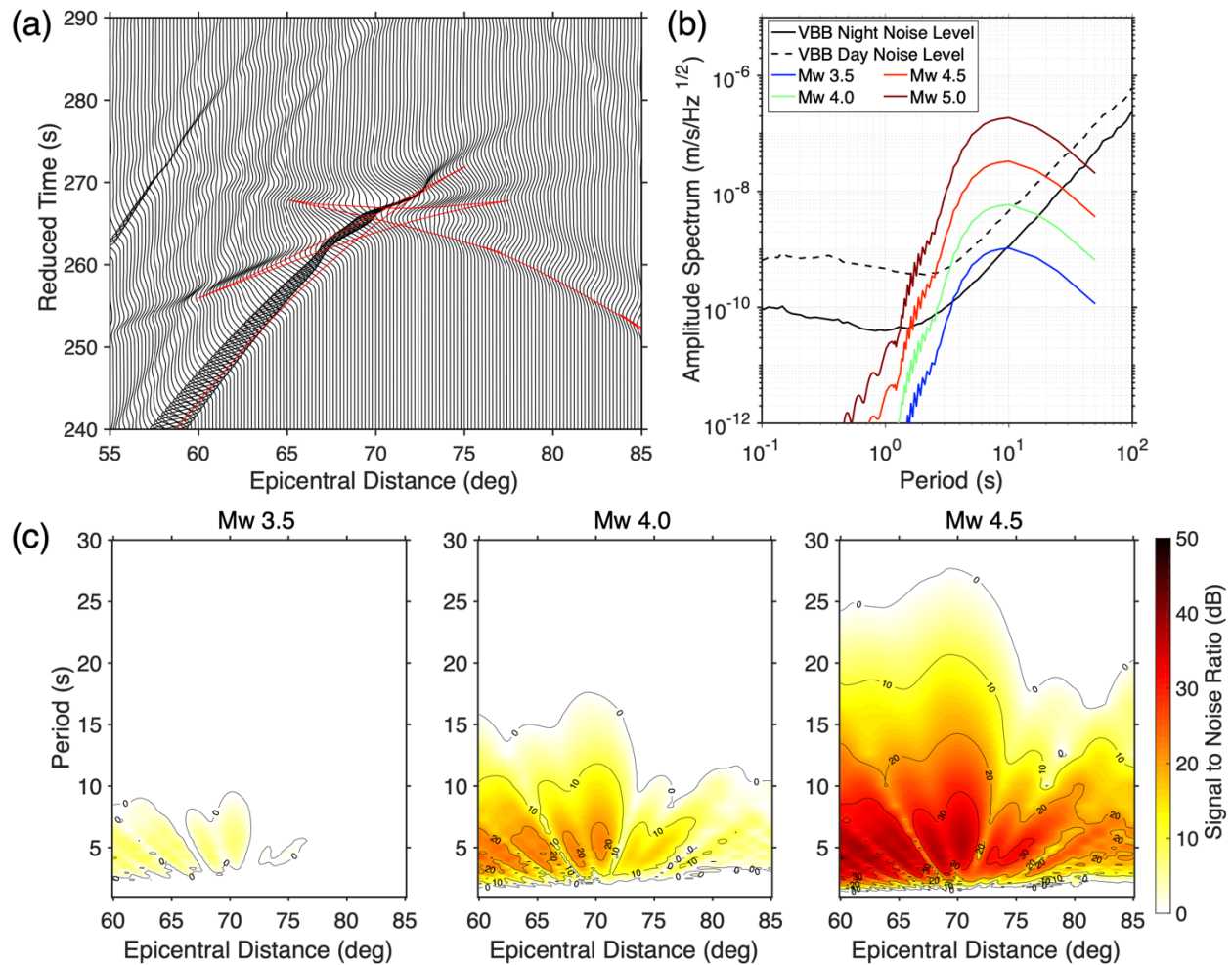
Fig. S4-10. Detectability of S triplication. (a) The synthetic waveforms of S triplications on the transverse component using the EH45TcoldCrust1 model (29). The synthetics are bandpass filtered between 1 and 100 s. (b) The amplitude spectra of S triplications for different event magnitudes. The amplitude spectra are computed from a 50 s time window centered around the triplication at 70 degrees. The average noise level of VBB BHE and BHN are shown by the black curves. (c) The SNR of S triplications for different event magnitudes. The magnitude threshold is Mw 3.5. The period range is 1-25 s, and the distance range is 60-85 degrees to detect the S triplications.

4.5 Synthetic Tests for Polarization Filtering

We performed synthetic tests for the polarization filtering method described in the Methods section of "Polarization Filter". Here, we used the best-fitting model shown in Fig. 3A as an example. We computed AxiSEM synthetics using the seismic source shown in Fig. S1-13 and the same method described in the Methods section of "Synthetic Waveform Modeling". We first evaluated the polarization filtering method on the noise-free synthetics as a benchmark. The P triplications are largely unchanged by the polarization filtering because they are predominantly polarized on the vertical component (Fig. S4-11). The S triplications are partitioned into the radial and transverse components with stronger amplitudes on the radial component in this case. Polarization filtering introduces a non-linear effect on the waveforms (see eq. 2) which amplifies the amplitude differences between the radial and transverse components (Fig. S4-12 and Fig. S4-13). This suggests that the polarization filter can enhance the S waves on one of the horizontal components at the cost of suppressing them on the other component. In our data analysis, we only picked S waves on the component with the larger SNR (see Methods section of "Data Processing Steps and Phase Identification"). Therefore, this ensures that the polarization filter enhanced the S triplications in the data. We note that the polarization filtering technique can potentially introduce amplitude distortions to the body waves, but these distortions predominantly exist on the horizontal components. However, the travel-time and phase information of the body waves are not affected by the polarization filter. Therefore, this limitation would not affect our overall conclusions on the '1000' discontinuity derived from the waveform modeling.

Next, we experimented with the noise-added synthetics. We generated realistic noises using the nighttime noise spectra of SEIS-VBB (Fig. S4-8) on the vertical and horizontal components. Then, we summed the vertical and horizontal noises with the synthetic waveforms on the

corresponding components. The clean and noise-added synthetics were bandpass filtered between 0.3-0.9 Hz. We introduced three levels of noise to the synthetics with SNR values of 2, 4 and 51. These SNR values were chosen to mimic the realistic noise levels in the data (Table S1-1). Finally, we applied polarization filtering to the noisy synthetics and compared the waveforms before and after filtering (Fig. S4-11 to Fig. S4-13).

On the vertical component (Fig. S4-11), we find that noise is effectively suppressed by the polarization filter even when the noise level is high (SNR=2). Crustal phases that arrive immediately after the P triplication have smaller amplitudes, thus are more easily obscured by the noise. As a result, these crustal phases tend to lose their rectilinear polarizations and can end up being suppressed by the polarization filter (Fig. S4-11b). Next, we tested the polarization filter for S triplications on the transverse and radial components. Transverse synthetics are decoupled from the other two components, so the polarization filter generally works best on this component and can suppress even the large-amplitude noise (Fig. S4-12). Similar to the vertical component, the radial component also displays S-to-P converted crustal phases (Fig. S4-13a). These crustal phases, together with the noise, are suppressed by the polarization filter (Fig. S4-13b). Based on this synthetic test, we conclude that our polarization filtering method can suppress random background noise and also low-amplitude crustal phases in the data, thereby enhancing the SNR of both P and S triplications.
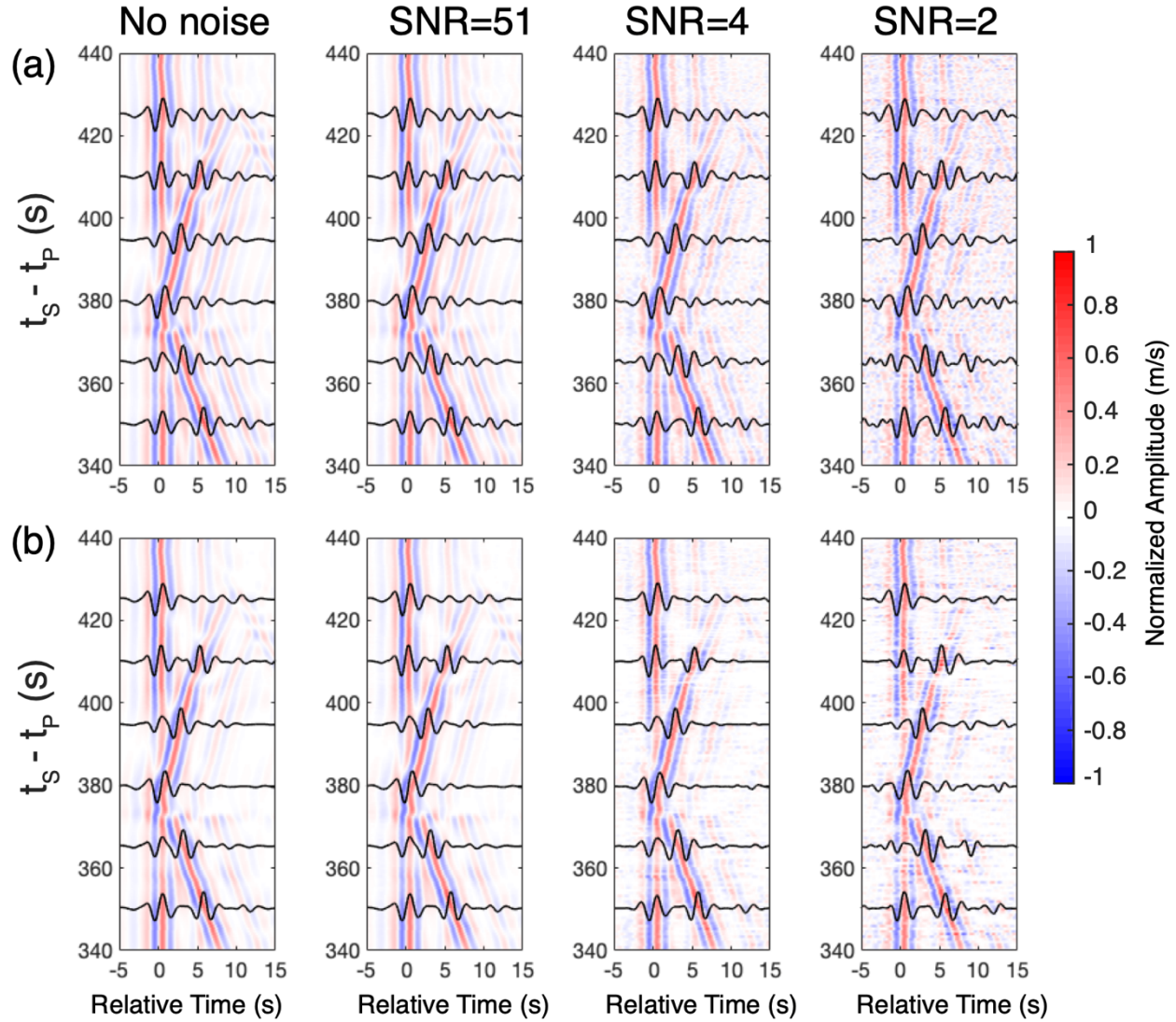
Fig. S4-11. Synthetic tests for the polarization filtering of P triplications on the vertical component. (a) P triplications before polarization filtering. The left panels contain the synthetics without any noise. Random noises are added to the clean synthetics with SNR values of 51, 4 and 2 from the second to fourth panels. All synthetics are bandpass filtered between 0.3 Hz and 0.9 Hz. The background color denotes synthetics across the entire distance range. Black curves highlight the synthetic waveforms at certain epicentral distances. (b) P triplications after polarization filtering.

Fig. S4-12. Synthetic tests for the polarization filtering of S triplications on the transverse component. S triplications (a) before and (b) after polarization filtering. Legends are the same as Fig. S4-11.
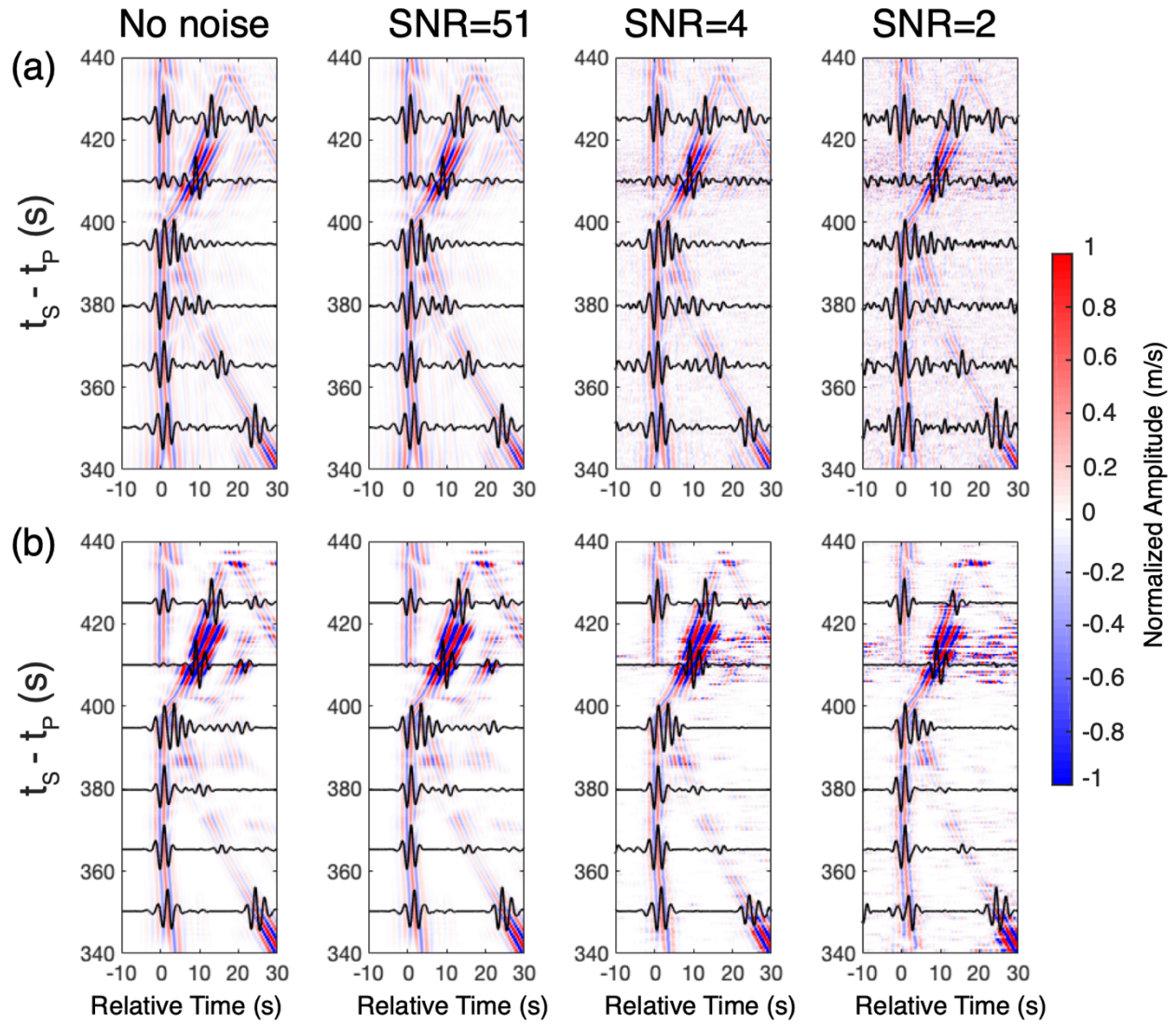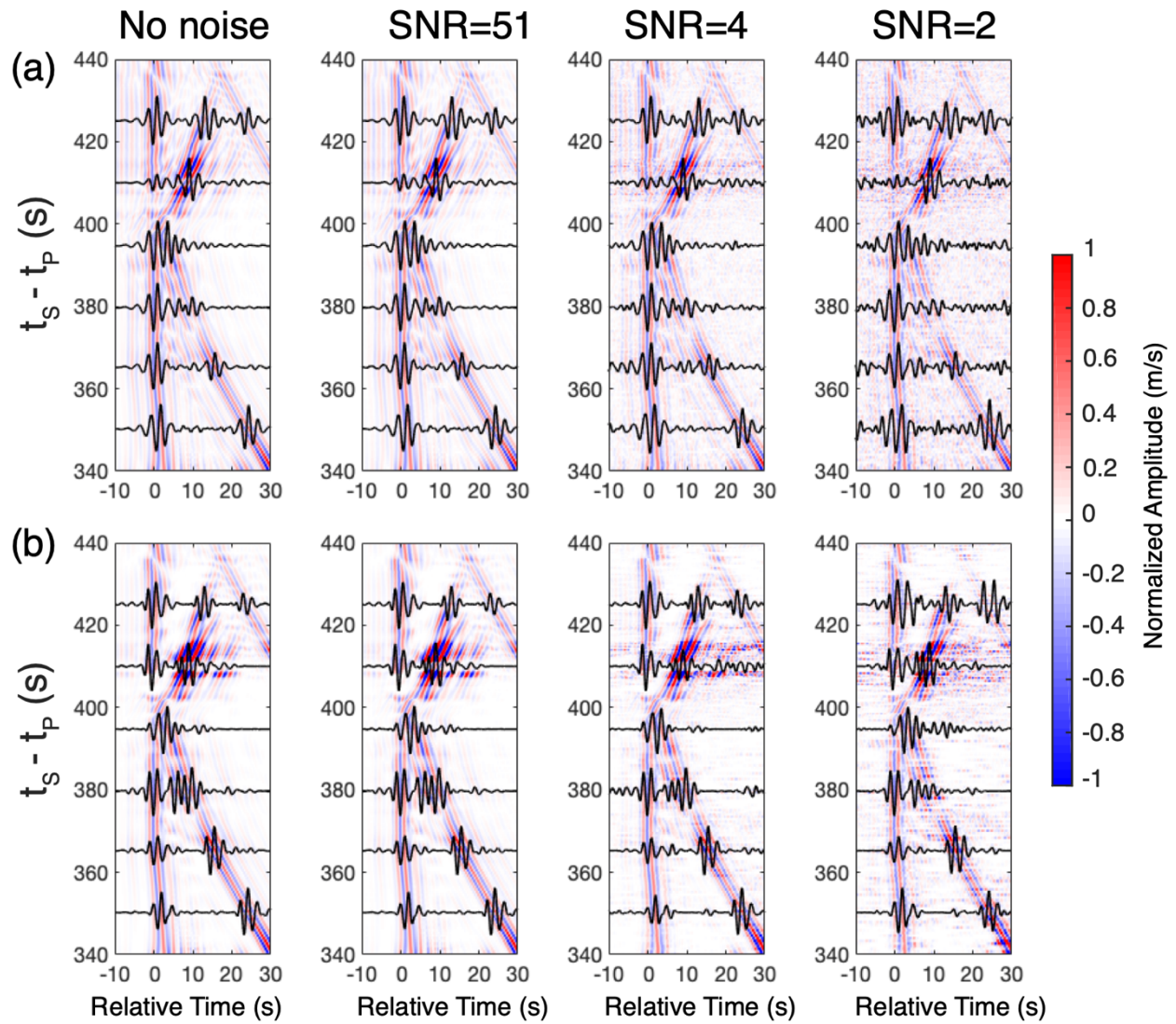
Fig. S4-13. Synthetic tests for the polarization filtering of S triplications on the radial component. S triplications (a) before and (b) after polarization filtering. Legends are the same as Fig. S4-11.

4.6 Evaluating the Interference of Crustal and Depth Phases

As described in the Methods section of "Synthetic Waveform Modeling", we suppressed crustal conversions/reflections and depth phases in the synthetics by artificially increasing the crustal attenuation. We also muted the mantle attenuation so that the frequency content of the S wave can match the data. Here, we evaluate the potential interference of crustal and depth phases by using a more realistic attenuation model from InSight_KKS21_GP model (1–3). The InSight_KKS21_GP model has weaker crustal attenuation and stronger mantle attenuation compared to the attenuation structure used in our waveform modeling (Fig. S4-14). Currently, no attenuation model is directly constrained by the InSight seismic data, including the InSight_KKS21_GP model. Most attenuation models of Mars are scaled from PREM (35) which does not necessarily represent the real structure of Mars.

After using the arguably more realistic attenuation structure from InSight_KKS21_GP model, the crustal phases and depth phases start to emerge in the synthetics, but their amplitudes are still smaller than the P and S triplications. On the vertical component (Fig. S4-15), we see the P-to-S conversion at 8 km depth (P8s) and the depth phase (pP) arriving 5 s and 12 s after the first P-arrival, respectively. Both P8s and pP phases show triplications due to their interactions with the '1000' discontinuity. The P8s phase can potentially interfere with the P triplication, but the pP phase arrives later than all the P triplications. However, these phases have smaller amplitudes and can easily lose their rectilinear polarizations due to the noise contaminations. Our synthetic tests show that we can effectively suppress the P8s and pP phases using the polarization filter especially for the low SNR cases (Fig. S4-15).

On the horizontal components (Fig. S4-16 and Fig. S4-17), we see the crustal S-reflection at 8 km depth (SSv8s) and the depth phase (sS) arriving 10 s and 22 s after the first S-arrival,

respectively. It is difficult to suppress the SSv8s phase when SNR is high (e.g, second column in Fig. S4-16). This is consistent with our observations of the crustal S-reflections in the two large events S1094b (Fig. S1-1) and S1102a (Fig. S1-3), but they do not interfere with the S triplications in these two events. When SNR is low (e.g, third and fourth columns in Fig. S4-16), we can effectively suppress the SSv8s and sS phases using the polarization filter because their rectilinear polarizations are obscured by the noise. From this synthetic test, we demonstrate that our polarization filter method can suppress the interference of crustal conversions/reflections and depth phases in the data, thus ensuring the robustness of the observations of mantle triplications.
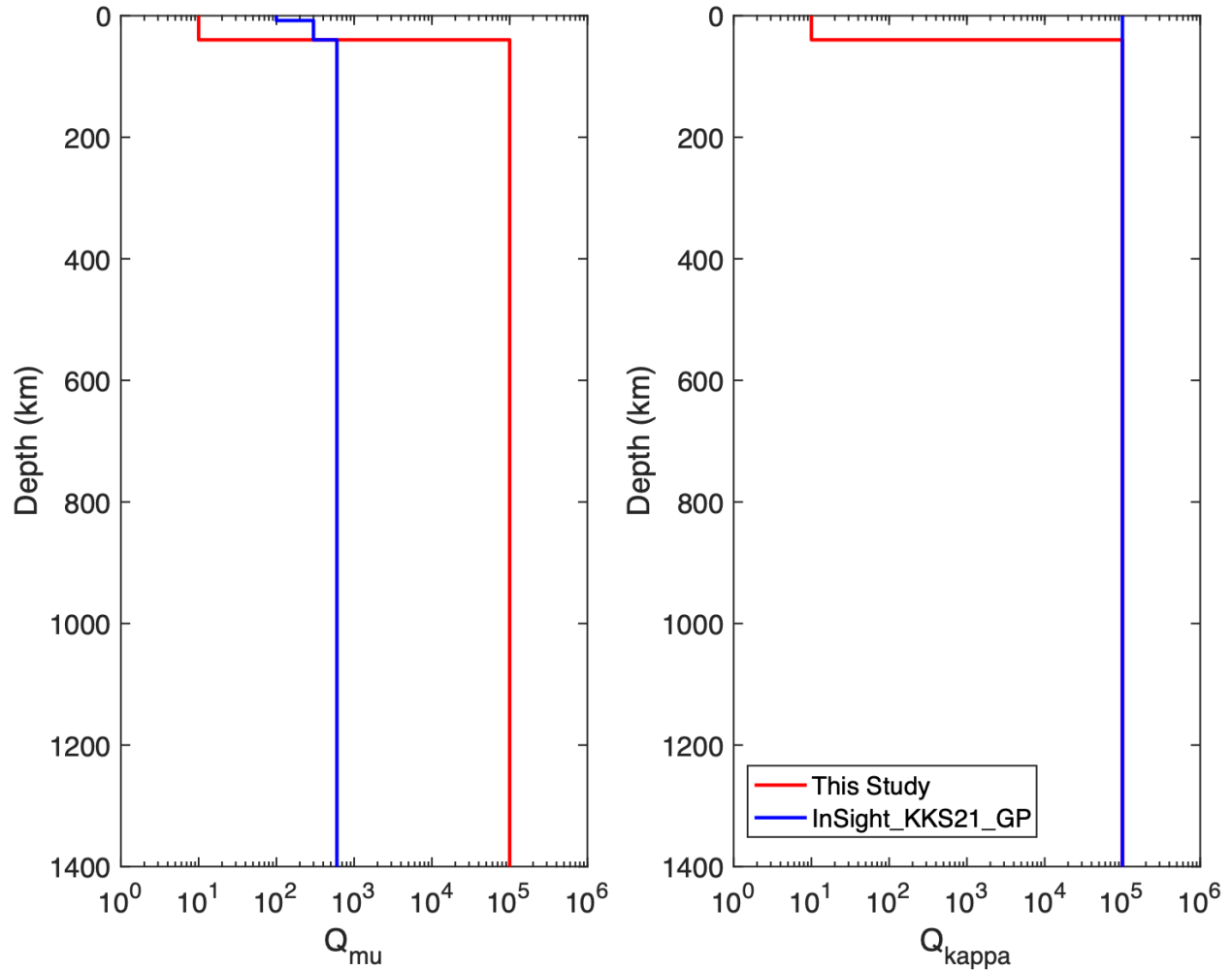
Fig. S4-14. Comparisons of the attenuation structure from InSight_KKS21_GP model (blue) and that used in this study (red). Note that our attenuation structure more easily fits the polarization-filtered triplicated waveforms, but this is not meant to represent the real attenuation structure of Mars.

Fig. S4-15. Synthetic tests for the polarization filtering of P triplications on the vertical component. Same as Fig. S4-11 but with the attenuation structure from InSight_KKS21_GP model. The black arrows highlight the arrival times of P-to-S conversions (P8s) and depth phase (pP) assuming a 30 km source depth.

Fig. S4-16. Synthetic tests for the polarization filtering of S triplications on the transverse component. Same as Fig. S4-12 but with the attenuation structure from InSight_KKS21_GP model. The black arrows highlight the arrival times of crustal reflections (SSv8s) and depth phase (sS) assuming a 30 km source depth.
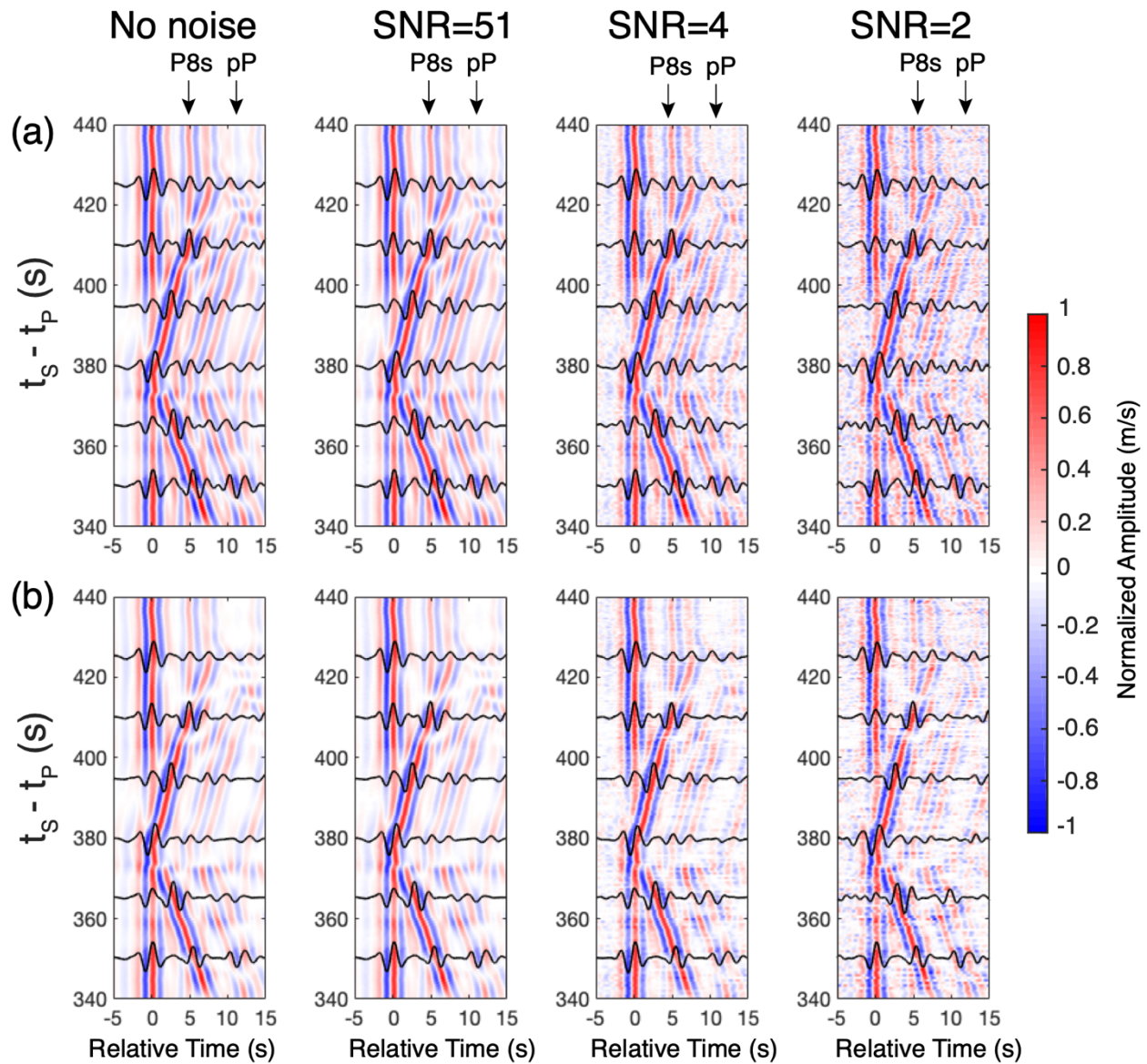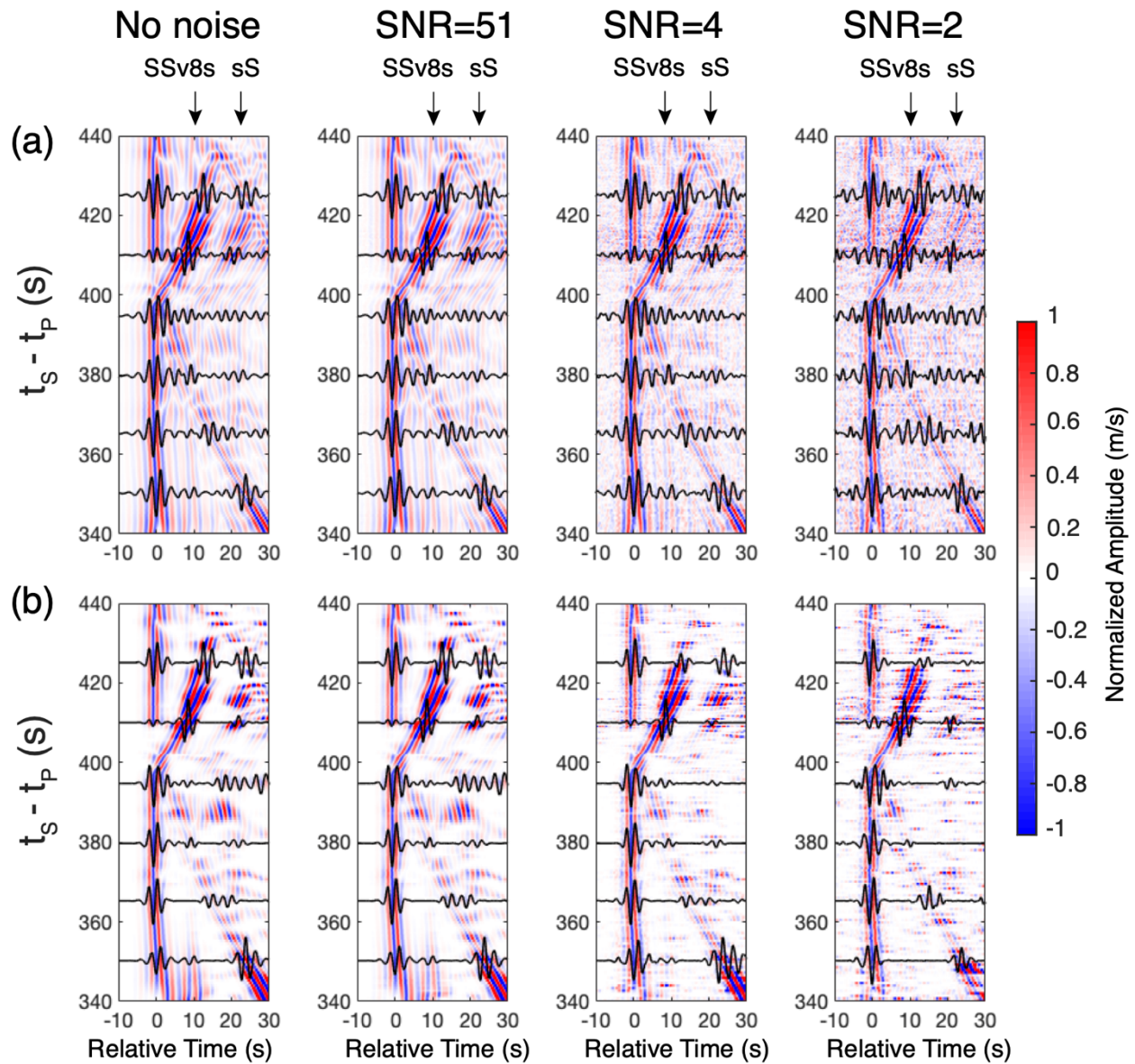
Fig. S4-17. Synthetic tests for the polarization filtering of S triplications on the radial component. Same as Fig. S4-13 but with the attenuation structure from InSight_KKS21_GP model. The black arrows highlight the arrival times of crustal reflections (SSv8s) and depth phase (sS) assuming a 30 km source depth.
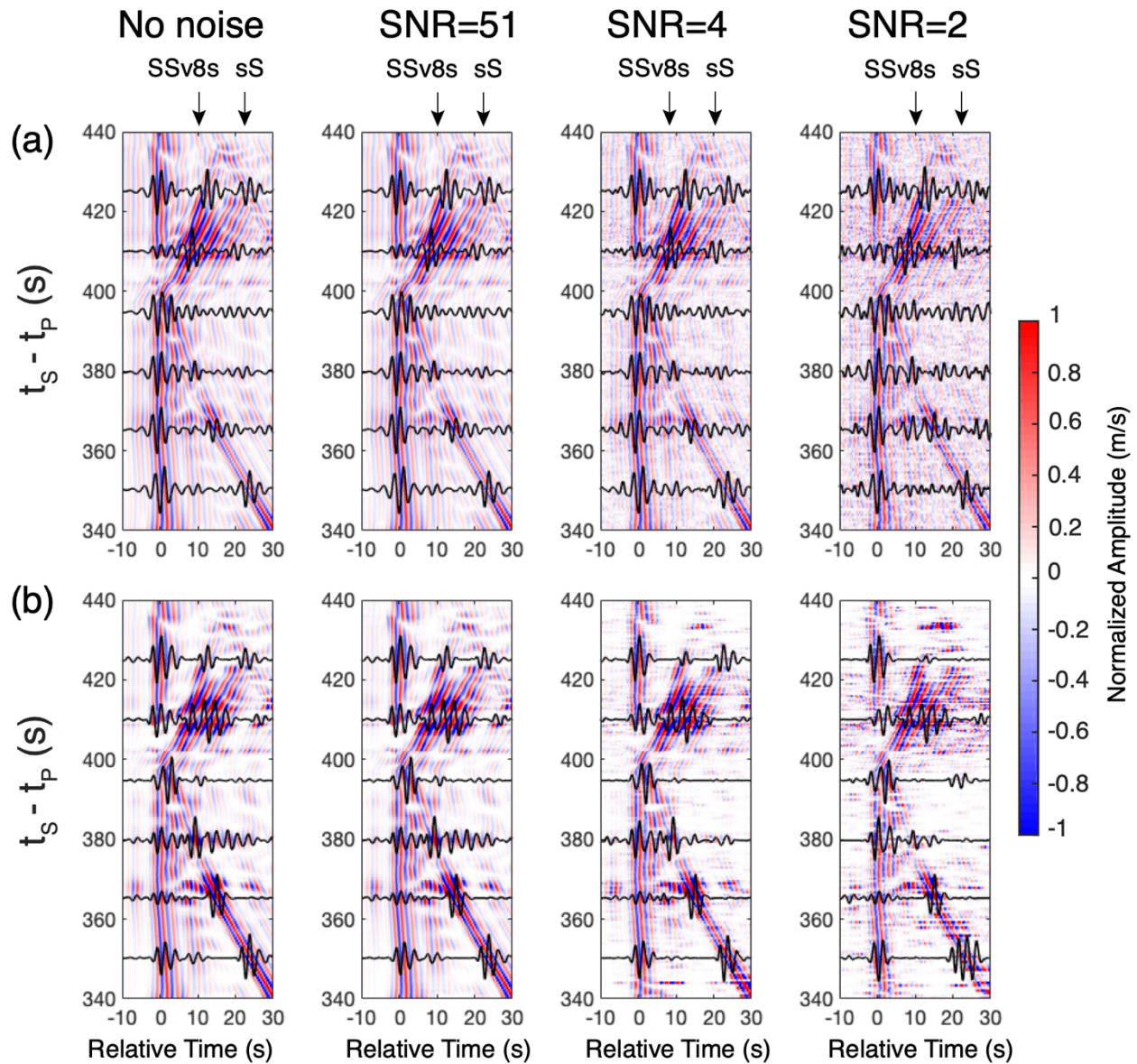
SI5. Mineralogy of the Mantle Transition Zone

5.1 Effects of Bulk Composition on the Post-olivine Transition

Simplified composition models were created by mixing chondritic compositions (36) to systematically test the effects of composition, specifically the Mg#, Mg/Si ratio and the enrichment of refractory elements, on the '1000' depth. The Mg# was varied between 72 and 82 (Table S5-1), by lowering the FeO content, to cover a wide range of values that include the Mg# proposed in various Martian compositions (4–8, 10). The resulting '1000' depth becomes shallower with decreasing Mg# (higher FeO) as it is shown in Fig. S5-1a. This is a simple consequence of the pressure of the post-olivine transition decreasing with increasing Fe_2SiO_4 content [e.g., (14)].

In a second set of calculations, we fixed Mg# at 76 and varied the Mg/Si ratio by changing the proportion of H chondrite relative to CI (Table S5-2). Decreasing the Mg/Si ratio and thus increasing the proportion of H chondrite, also moves the '1000' to shallower depths, although to a lesser extent than decreasing the Mg# (Fig. 5-1b). In this case, the change in the '1000' depth is driven by changes in the proportions of garnet and pyroxene, which have, respectively, higher and lower Fe/Mg ratios relative to olivine. Finally, we considered the possibility that refractory elements (RE: Ca, Al) are enriched in the Martian mantle relative to major lithophile elements (Si, Mg) and chondrites as suggested by (8). The chondrite-normalized concentration of RE was varied from 1.0 (4) to 1.20 (Table S5-3). An enrichment of RE has no detectable effect on the '1000' depth (Fig. S5-1c).

The effects of composition trade-off with the mantle temperature (Fig. S5-2). A bulk composition with a low Mg# (e.g., 74) would allow for high mantle temperatures (~1750 K) to be compatible with a '1000' depth of 1006 km (12.78 GPa), while a high Mg# (Mg# > 80) would require a mantle temperature lower than 1700 K to keep the '1000' at the same depth.
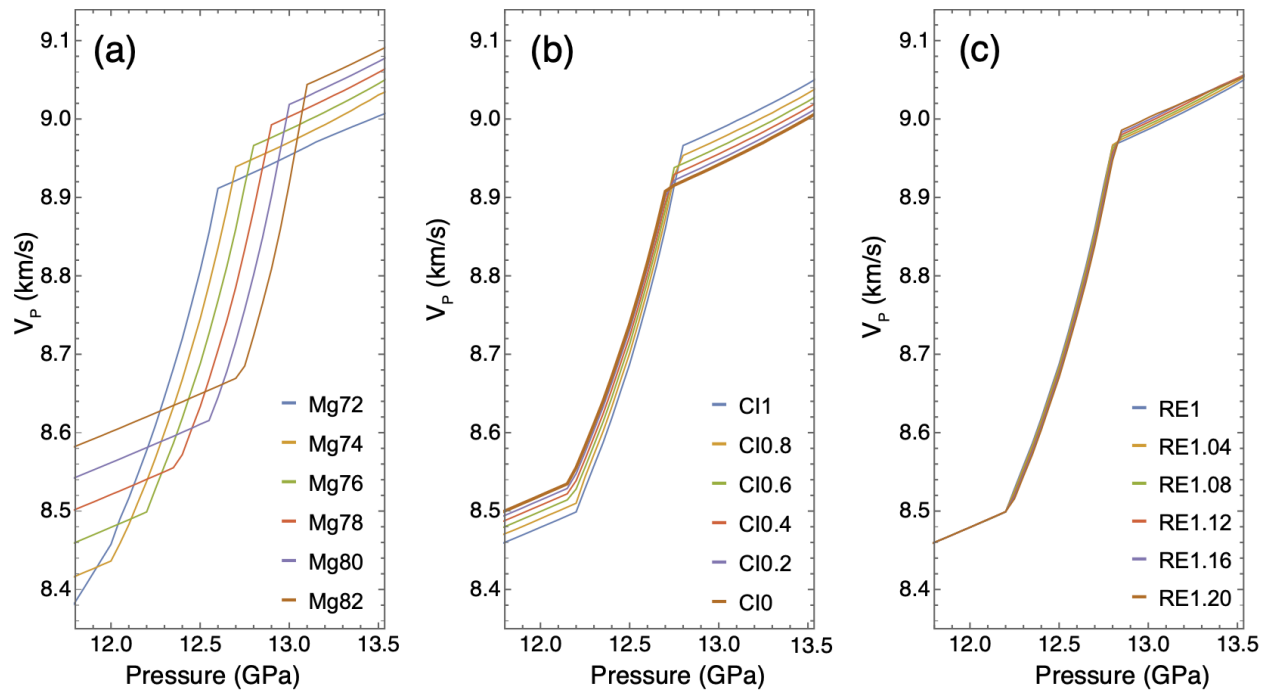
Fig. S5-1. Effects of bulk composition on the '1000' depth: (a) the Mg#, (b) Mg/Si ratio varied from 1.03 for CI1 to 0.96 for CI0, corresponding to a H chondritic composition, (c) refractory elements varied between RE=1, corresponding to the chondritic abundance used by DW85, and RE=1.20, which is slightly higher than the value of 1.16 used in the YM20 composition. In panel (a) the Mg/Si ratio was kept at CI1 and the refractory elements at RE=1. In panel (b) the Mg# is set to 76 and the refractory elements at RE=1. When varying the refractory elements in panel (c), the Mg# was set to 76 and the Mg/Si ratio was kept at CI1.
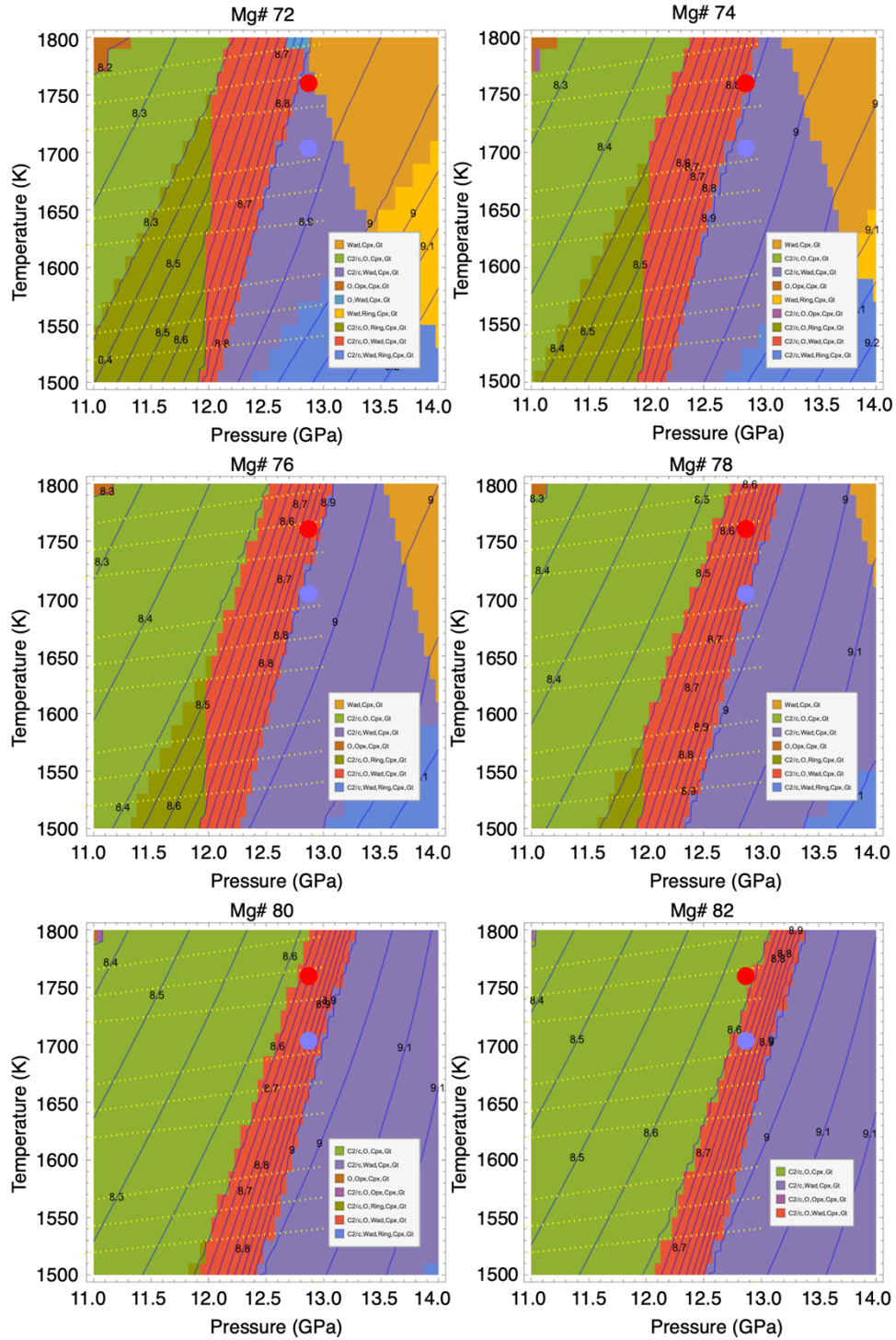
Fig. S5-2. Trade-off between the mantle potential temperature and mantle composition (Mg#) to keep the '1000' at a depth of 1006 km (12.78 GPa). The contour lines indicate the compressional wave velocity in km/s. The yellow dotted lines indicate mantle adiabats, assuming various potential temperatures and adiabatic gradients (see Fig. S2-1 for additional details). The blue and red filled circles indicate the minimum and maximum temperature, respectively, that were obtained in thermal evolution models (3, 37) at 12.78 GPa.

Table S5-1. Compositions (in wt%) with variable Mg#: The compositions are based on (4, 7) but the Mg# was varied between 72 and 82.

	Mg# 72	Mg# 74	Mg# 76	Mg# 78	Mg# 80	Mg# 82
SiO_2	43.341	44.228	45.102	45.963	46.813	47.650
Al_2O_3	3.0051	3.0665	3.1271	3.1869	3.2458	3.3039
FeO	20.764	19.143	17.546	15.971	14.417	12.886
MgO	29.953	30.566	31.170	31.765	32.352	32.931
CaO	2.4135	2.4628	2.5115	2.5595	2.6068	2.6534
Na_2O	0.5231	0.5338	0.5443	0.5547	0.5650	0.5751

Table S5-2. Compositions with variable Mg/Si ratio: The compositions are based on (7) with a Mg# = 76, but the Mg/Si ratio was varied between that of CI chondrites (CI = 1) and H chondrites (CI = 0).

	CI = 1	CI = 0.8	CI = 0.6	CI = 0.4	CI = 0.2	CI = 0
SiO2	45.102	45.661	46.125	46.517	46.852	47.141
Al2O3	3.1271	3.033	2.9549	2.889	2.8326	2.7839
FeO	17.546	17.407	17.292	17.194	17.111	17.04
MgO	31.17	30.923	30.718	30.546	30.398	30.27
CaO	2.5115	2.4481	2.3956	2.3512	2.3133	2.2805
Na2O	0.54435	0.52797	0.51436	0.50289	0.49308	0.4846

Table S5-3. Compositions with variable refractory element concentrations: The Mg# was kept constant at 76, but the refractory elements (RE) were varied between 1 and 1.20. RE = 1 corresponds to the chondritic abundance assumed by (4, 6–8). RE = 1.16 is similar to the level of RE enrichment assumed by (8). Na_2O increases with refractory elements to conserve the Na_2O/Al_2O_3 ratio of shergottites and for consistency with the degree of alkali-depletion inferred from GRS K/Th ratios.

	RE = 1	RE = 1.04	RE = 1.08	RE = 1.12	RE = 1.16	RE = 1.20
SiO2	45.102	44.99	44.88	44.769	44.66	44.551
Al2O3	3.1271	3.2442	3.3607	3.4766	3.5919	3.7067
FeO	17.546	17.502	17.459	17.417	17.374	17.331
MgO	31.17	31.093	31.016	30.94	30.864	30.789
CaO	2.5115	2.6055	2.699	2.7921	2.8848	2.977
Na2O	0.54435	0.56473	0.585	0.60518	0.62526	0.64524

5.2 Effects of Water on the Post-olivine Transition

Similar to the case of Fe and Mg, the incorporation of H_2O as hydroxyl (OH^-) into mantle minerals affects their properties. Water solubility in olivine is limited to 1 wt % at the pressures of wadsleyite formation, and decreases with increasing temperature (17, 38, 39) (Fig. S5-3). In contrast, wadsleyite can accommodate up to 3.1 wt.% H_2O (40). The presence of water lowers the post-olivine transition pressure in both Fe-free and Fe-bearing systems by stabilizing the high-pressure phase (15–17, 41). The presence of water below the saturation limit also broadens the transition, by lowering the pressure where wadsleyite first appears without significantly changing the pressure where olivine disappears (16–18). In addition to water, ferric iron could also contribute to broadening of the post-olivine transition [e.g., (42)]. However, the bulk of Mars' deep mantle is likely to be reduced (43) to an oxygen fugacity similar to the conditions studied experimentally by (14). While oxidized regions have been suggested in the uppermost Martian mantle (44), Fe^{3+} would be preferentially accommodated into coexisting garnet rather than in olivine or wadsleyite, which can then be assumed to contain iron predominantly as Fe^{2+} at MTZ conditions. In the following, we therefore concentrate on the possible effect of water.

To quantitatively investigate the effect of water on the post-olivine transition, we have parameterized thermodynamic models of the two phases, following the recommendations of (17). We assume that mixing in olivine can be described by the following formula: $[Mg,Fe][Mg,Fe,v]Si(O,OH)_2O_2$, where the mixing entropy is given by the sites in square brackets only (the occupancies of the sites in rounded brackets are dictated by local ordering). For wadsleyite, we assume that mixing is described by the following formula: $[Mg,Fe]_{1.5}[Mg,Fe,v]_{0.5}Si(O,OH)O_3$. "v" in these expressions represents site vacancies.

Interactions between independent endmembers are described using a regular solution model. Each model has four endmembers: $[Mg][Mg]SiO_4$, $[Fe][Fe]SiO_4$, $[Mg][Fe]SiO_4$ and $[Mg][v]SiO_4H_2$ for olivine, and $[Mg]_{1.5}[Mg]_{0.5}SiO4$, $[Fe]_{1.5}[Fe]_{0.5}SiO_4$, $[Mg]_{1.5}[Fe]_{0.5}SiO_4$ and $[Mg]_{1.5}[v]_{0.5}SiO_4H$ for wadsleyite. Interactions between vacancies and Mg or Fe are assumed to be ideal, while interactions between Mg and Fe are assumed to be equal to 7.81322/2 and 16.74718/2 kJ/mol per site respectively (22). For example, the interaction energy between $[Fe]_{1.5}[Fe]_{0.5}SiO_4$ and $[Mg]_{1.5}[v]_{0.5}SiO_4H$ wadsleyite is 16.74718 * 0.75 kJ/mol.

The Gibbs energy of Mg-wadsleyite and Fe-wadsleyite endmembers are defined relative to their olivine counterparts so as to agree with the Stixrude and Lithgow-Bertelloni datasets (22) at 14 GPa and 1673 K:

$$G(mwd) = G(fo) + 19965 + 5.27354*T - 2.06062e\text{-}6*P \tag{13}$$

$$G(fwd) = G(fa) - 3837 + 10.89652*T - 2.47956e\text{-}06*P \tag{14}$$

where G is in J/mol, T is in K and P is in Pa.

The Gibbs energy of the ordered compounds is determined assuming a negligible energy of ordering:

$$G([Mg][Fe]SiO_4, ol) = 0.5 * G(fo) + 0.5 * G(fa) \tag{15}$$

$$G([Mg]_{1.5}[Fe]_{0.5}SiO_4, wad) = 0.75 * G(mwd) + 0.25 * G(fwd) \tag{16}$$

The Gibbs energy of the $Mg_{1.5}SiO_4H$ wadsleyite endmember is defined relative to forsterite and the $MgSiO_4H_2$ olivine endmember in order to approximately fit the compositions of olivine and wadsleyite at water saturation in the $MgO\text{-}SiO_2\text{-}H_2O$ (MSH) system:

$$G(Mg_{1.5}SiO_4H, wad) = (G(MgSiO_4H_2, ol) + G(fo))/2 - 16989 + 3.60622e\text{-}07*P \tag{17}$$

The temperature dependence of the $Mg_{1.5}SiO_4H$-forming reaction is unknown and assumed to be equal to zero. A comparison between the model and experimental data in the MSH system is shown in Fig. S5-3.

This model is used to predict the effect of H_2O on the post-olivine transition across the FeO-MgO-SiO_2-H_2O (FMSH) system. More iron rich bulk compositions exhibit greater midpoint depression and transition broadening (Fig. S5-4a,b). Here, we define the midpoint of the transition as the point at which there are equal numbers of moles of olivine and wadsleyite (on a 4-oxygen basis). For water contents lower than around 1000 ppm, the depression of the transition midpoint between Mg# of 70 and 100 (covering the full range of wadsleyite stability) at 1773 K is only around 0.1 GPa (Fig. S5-4a). The addition of H_2O leads to increasing asymmetry of the transition (Fig. S5-4c), such that the reaction progress is slow near to the wadsleyite-in boundary. This would render the onset of the transition difficult to be seismically observed, making it appear narrower.

The actual broadening of the transition is limited by water saturation in olivine. Once olivine is saturated, a fluid phase becomes stable, causing the transition to become narrower, as observed experimentally by (41). The amount of hydrogen in water-saturated olivine at high pressure was investigated by (39) (inset of Fig. S5-4d). The depression of the midpoint of the post-olivine transition at water saturation decreases from around 0.4 GPa at 1473-1673 K to 0.2 GPa at 1773 K and < 0.1 GPa at >1873K (Fig. S5-4d). We note here that our estimate of 0.4 GPa at 1473 K is about half that of (17). This is largely because they estimated the content of H_2O in olivine at water saturation only from two experimental data points from (38), while our model is constructed to also account for experimental data from (39) and model considerations (45). The discrepancy is reduced at higher temperatures, and at the most likely temperatures for the mantle, our model agrees well with the experimental data from (38, 39), and the model of (17).

The compositions of Martian meteorites suggest that their mantle sources contained 70-300 ppm H_2O (46, 47). Even if we assume that pyroxene and garnet contain negligible water, this probably limits water in olivine to around 500 ppm. Comparing these estimates with Fig. S5-4 (a and b) suggests that the midpoint depression of the post-olivine transition is probably less than 0.1 GPa. We note that even without the meteoritic constraints, the water-induced depression of the transition midpoint is unlikely to exceed ~0.4 GPa (corresponding to around 30 km in Mars mantle) because of the limited solubility of water in olivine. Once olivine is saturated in water, additional water will form a free fluid phase, which will buffer the pressure of the post-olivine reaction. Water is therefore unlikely to have a significant influence on the depth of the post-olivine transition.
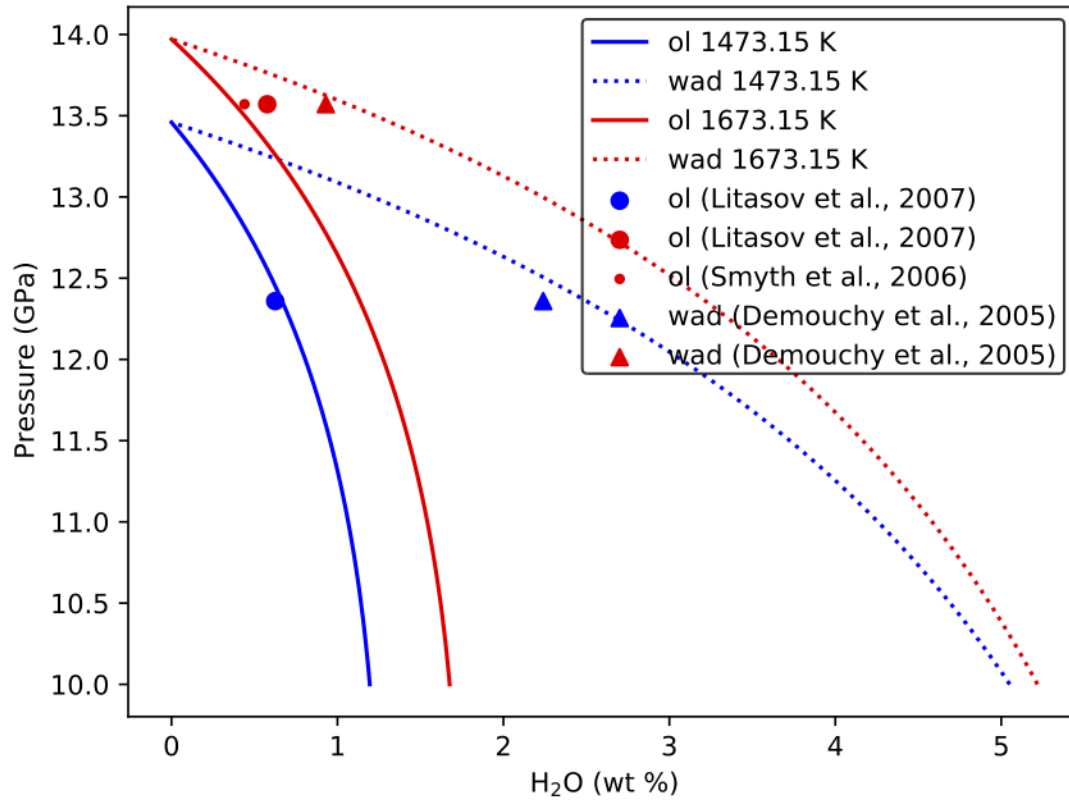
Fig. S5-3. Comparison between our preferred model for water solubility in olivine and wadsleyite as a function of pressure, with experimental data from the literature in the system MgO-SiO_2-H_2O. See text in SI 5.2 for details of the model.
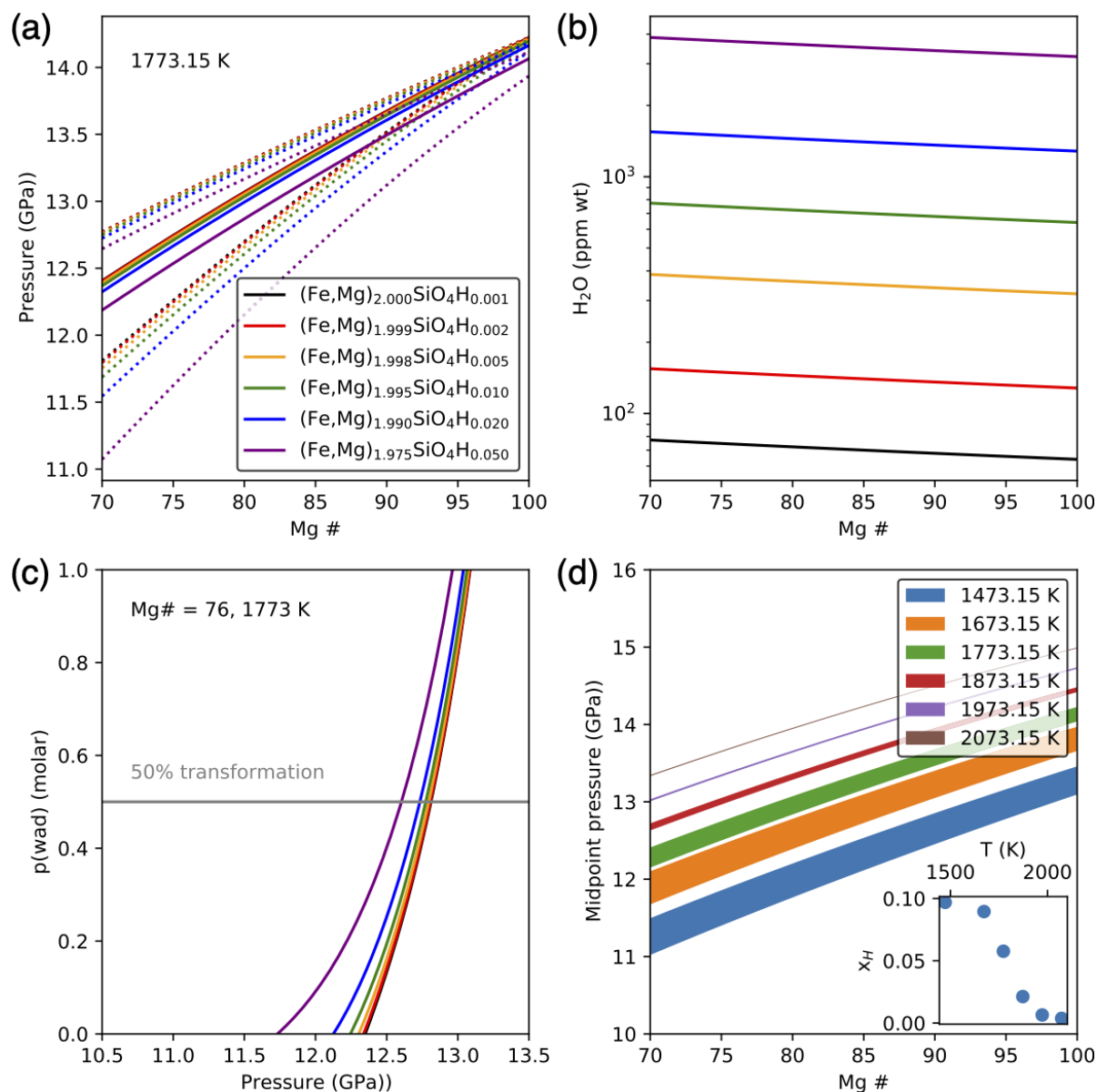
Fig. S5-4. The effect of H_2O on the post-olivine transition. Top left (a): The post-olivine transition at 1773.15 K for a range of H_2O contents. Each line corresponds to a different bulk composition. Dotted lines delimit the transition, and solid lines mark where the moles of olivine and wadsleyite are equal. Top right (b): The amount of water in each bulk composition, expressed in ppm wt. Bottom left (c): The proportion of wadsleyite over the transition for different water contents at Mg# = 76 and 1773 K. Note that although the starting pressure of the transition is depressed significantly at > 1000 ppm weight H_2O, the center point of the transformation (in terms of the proportion of wadsleyite) is less significantly affected. Bottom right (d): Range of transition midpoints (as defined by equal amounts of olivine and wadsleyite) between dry and water-saturated conditions in olivine. The bottom of each filled region corresponds to water-saturated conditions. Inset shows the hydrogen concentration at water saturation according to (96). The transition on the far-left hand side of the plot (at high Fe contents) is metastable with respect to ringwoodite+olivine.

Supplementary References

1. S. C. Stähler, *et al.*, Seismic detection of the martian core. *Science (1979)* **373**, 443–448 (2021).

2. A. Khan, *et al.*, Upper mantle structure of Mars from InSight seismic data. *Science (1979)* **373**, 434–438 (2021).

3. B. Knapmeyer-Endrun, *et al.*, Thickness and structure of the martian crust from InSight seismic data. *Science (1979)* **373**, 438–443 (2021).

4. G. Dreibus, H. Wänke, Mars, a volatile-rich planet. *Meteoritics* **20**, 367–381 (1985).

5. A. Khan, J. A. D. Connolly, Constraining the composition and thermal state of Mars from inversion of geophysical data. *J Geophys Res Planets* **113**, 7003 (2008).

6. K. Lodders, B. Fegley, An oxygen isotope model for the composition of Mars. *Icarus* **126**, 373–394 (1997).

7. G. J. Taylor, The bulk composition of Mars. *Chemie der Erde* **73**, 401–420 (2013).

8. T. Yoshizaki, W. F. McDonough, The composition of Mars. *Geochim Cosmochim Acta* **273**, 137–162 (2020).

9. A. C. Plesa, *et al.*, How large are present-day heat flux variations across the surface of Mars? *J Geophys Res Planets* **121**, 2386–2403 (2016).

10. C. Sanloup, A. Jambon, P. Gillet, A simple chondritic model of Mars. *Physics of the Earth and Planetary Interiors* **112**, 43–54 (1999).

11. G. R. Helffrich, B. J. Wood, 410 km discontinuity sharpness and the form of the olivine α-β phase diagram: resolution of apparent seismic contradictions. *Geophys J Int* **126**, F7–F12 (1996).

12. C. S. Zha, T. S. Duffy, R. T. Downs, H. K. Mao, R. J. Hemley, Sound velocity and elasticity of single-crystal forsterite to 16 GPa. *Journal of Geophysical Research B: Solid Earth* **101**, 17535–17545 (1996).

13. L. Stixrude, Structure and sharpness of phase transitions and mantle discontinuities. *J Geophys Res Solid Earth* **102**, 14835–14852 (1997).

14. D. J. Frost, The structure and sharpness of $(Mg,Fe)_2SiO_4$ phase transformations in the transition zone. *Earth Planet Sci Lett* **216**, 313–328 (2003).

15. B. J. Wood, The effect of H_2O on the 410-kilometer seismic discontinuity. *Science (1979)* **268**, 74–76 (1995).

16. J. R. Smyth, D. J. Frost, The effect of water on the 410-km discontinuity: An experimental study. *Geophys Res Lett* **29**, 123-1-123–4 (2002).

17. D. J. Frost, D. Dolejš, Experimental determination of the effect of H_2O on the 410-km seismic discontinuity. *Earth Planet Sci Lett* **256**, 182–195 (2007).

18. V. N. Zharkov, T. v. Gudkova, Seismic model of Mars: Effects of hydration. *Planet Space Sci* **104**, 270–278 (2014).

19. T. Katsura, *et al.*, Olivine-wadsleyite transition in the system (Mg,Fe)2SiO4. *J Geophys Res Solid Earth* **109**, 2209 (2004).

20. J. W. Hernlund, On the interaction of the geotherm with a post-perovskite phase transition in the deep mantle. *Physics of the Earth and Planetary Interiors* **180**, 222–234 (2010).

21. H. M. Benz, J. E. Vidale, Sharpness of upper-mantle discontinuities determined from high-frequency reflections. *Nature* **365**, 147–150 (1993).

22. L. Stixrude, C. Lithgow-Bertelloni, Thermodynamics of mantle minerals - II. Phase equilibria. *Geophys J Int* **184**, 1180–1213 (2011).

23. P. Lognonné, *et al.*, SEIS: Insight's Seismic Experiment for Internal Structure of Mars. *Space Sci Rev* **215**, 1–170 (2019).

24. N. Murdoch, *et al.*, Evaluating the Wind-Induced Mechanical Noise on the InSight Seismometers. *Space Sci Rev* **211**, 429–455 (2017).

25. M. P. Panning, *et al.*, On-Deck Seismology: Lessons from InSight for Future Planetary Seismology. *J Geophys Res Planets* **125**, e2019JE006353 (2020).

26. J. R. Peterson, Observations and modeling of seismic background noise. *Open-File Report* (1993) https:/doi.org/10.3133/OFR93322 (July 29, 2021).

27. A. Friedrich, F. Krüger, K. Klinge, Ocean-generated microseismic noise located with the Gräfenberg array. *J Seismol* **2**, 47–64 (1998).

28. P. Lognonné, *et al.*, Constraints on the shallow elastic and anelastic structure of Mars from InSight seismic data. *Nat Geosci* **13**, 213–220 (2020).

29. A. Rivoldini, T. van Hoolst, O. Verhoeven, A. Mocquet, V. Dehant, Geodesy constraints on the interior structure and composition of Mars. *Icarus* **213**, 451–472 (2011).

30. A. M. Dziewonski, D. L. Anderson, Preliminary reference Earth model. *Physics of the Earth and Planetary Interiors* **25**, 297–356 (1981).

31. H. P. Crotwell, T. J. Owens, J. Ritsema, The TauP Toolkit: Flexible Seismic Travel-time and Ray-path Utilities. *Seismological Research Letters* **70**, 154–160 (1999).

32. J. F. Clinton, *et al.*, The Marsquake catalogue from InSight, sols 0–478. *Physics of the Earth and Planetary Interiors* **310**, 106595 (2021).

33. M. Böse, *et al.*, Magnitude Scales for Marsquakes Calibrated from InSight Data. *Bulletin of the Seismological Society of America* (2021) https:/doi.org/10.1785/0120210045 (July 17, 2021).

34. D. Giardini, *et al.*, The seismicity of Mars. *Nat Geosci* **13**, 205–212 (2020).

35. S. E. Smrekar, *et al.*, Pre-mission InSights on the Interior of Mars. *Space Sci Rev* **215** (2019).

36. J. T. Wasson, G. W. K. Allemeyn, Compositions of chondrites. *Philosophical Transactions of the Royal Society of London. Series A, Mathematical and Physical Sciences* **325**, 535–544 (1988).

37. A.-C. Plesa, *et al.*, The Thermal State and Interior Structure of Mars. *Geophys Res Lett* **45**, 12,198-12,209 (2018).

38. J. R. Smyth, D. J. Frost, F. Nestola, C. M. Holl, G. Bromiley, Olivine hydration in the deep upper mantle: Effects of temperature and silica activity. *Geophys Res Lett* **33**, 15301 (2006).

39. K. D. Litasov, E. Ohtani, H. Kagi, S. D. Jacobsen, S. Ghosh, Temperature dependence and mechanism of hydrogen incorporation in olivine at 12.5–14.0 GPa. *Geophys Res Lett* **34**, 16314 (2007).

40. T. Inoue, H. Yurimoto, Y. Kudoh, Hydrous modified spinel, Mg1.75SiH0.5O4: A new water reservoir in the mantle transition region. *Geophys Res Lett* **22**, 117–120 (1995).

41. J. Chen, T. Inoue, H. Yurimoto, D. J. Weidner, Effect of water on olivine-wadsleyite phase boundary in the (Mg,Fe)2SiO4 system. *Geophys Res Lett* **29**, 1875 (2002).

42. D. J. Frost, C. A. McCammon, The effect of oxygen fugacity on the olivine to wadsleyite transformation: Implications for remote sensing of mantle redox state at the 410 km seismic discontinuity. *American Mineralogist* **94**, 872–882 (2009).

43. M. Wadhwa, Redox State of Mars' Upper Mantle and Crust from Eu Anomalies in Shergottite Pyroxenes. *Science (1979)* **291**, 1527–1530 (2001).

44. J. Tuff, J. Wade, B. J. Wood, Volcanism on Mars controlled by early oxidation of the upper mantle. *Nature 2013 498:7454* **498**, 342–345 (2013).

45. R. Myhill, D. J. Frost, D. Novella, Hydrous melting and partitioning in and above the mantle transition zone: Insights from water-rich MgO–SiO2–H2O experiments. *Geochim Cosmochim Acta* **200**, 408–421 (2017).

46. F. M. McCubbin, *et al.*, Hydrous melting of the martian mantle produced both depleted and enriched shergottites. *Geology* **40**, 683–686 (2012).

47. F. A. Weis, *et al.*, Water content in the Martian mantle: A Nakhla perspective. *Geochim Cosmochim Acta* **212**, 84–98 (2017).